THERMAL METROLOGY OF POLYSILICON MEMS USING RAMAN SPECTROSCOPY

A Thesis Presented to

The Academic Faculty

By

Mark Richard Abel

In Partial Fulfillment of the Requirements for the Degree

Master of Science in Mechanical Engineering

Georgia Institute of Technology

August 2005

THERMAL METROLOGY OF POLYSILICON MEMS USING

RAMAN SPECTROSCOPY

Approved:

Dr. Samuel Graham, Chair
Mechanical Engineering
Georgia Institute of Technology

Dr. Zhuomin Zhang
Mechanical Engineering
Georgia Institute of Technology

Dr. Sean P. Kearney
Experimental Thermal-Fluid-Aero Sciences
Sandia National Laboratories

Date Approved: July 12th, 2005

ACKNOWLEDGEMENTS

I would like to thank my thesis advisor, Dr. Samuel Graham, and Dr. Sean Kearney of Sandia National Laboratories for the opportunity to work on this project and experience the complete research process. Without their continuous guidance and financial support throughout the process, I would not have been able to achieve my goal of a graduate degree in mechanical engineering. In addition, I would like to thank Dr. Zhuomin Zhang for serving on the thesis reading committee, and providing a review of my work.

Thank you to all of my fellow graduate students who provided assistance to me, both large and small, during my work, especially Adam Christensen, Erik Sunden, Ashante' Allen, Tanya Wright, and Abe Greenstein.

TABLE OF CONTENTS

LIST OF TABLES

LIST OF FIGURES

SUMMARY

The development of microscale and nanoscale devices has outpaced the development of metrology tools necessary for their complete characterization. In the area of thermal MEMS technology, accurate measurements across a broad range of temperatures with high spatial resolution are not trivial. Thermal MEMS are devices in which the control and manipulation of temperature is necessary to perform a desired function. This class of microdevices is important in technology as they are used in actuation, chemical sensing, nanolithography, thermal data storage, biological reactions and power generation. In order to properly design for reliability and performance issues amongst these devices and verify modeling accuracy, the temperature distribution under device operating conditions must be experimentally determined. Of the technologies which are candidates for thermal metrology, optical methods are ideal due to their nondestructive nature and potential for high spatial resolution using visible or ultra-violet radiation. Raman spectroscopy has the ability to provide absolute temperature measurements with spatial scales below 1 μm, which is sufficient for most MEMS devices.

In this work, a detailed study of Raman spectroscopy as an optical thermal metrology tool was performed. It is shown that a simple calibration of the Stokes shift with temperature yields a linear calibration for measurements up to 1000°C in polycrystalline Si. These linear coefficients were determined for polysilicon processed under various conditions (575-620ºC, B and P doping) to assess the effects of

microstructural variations on Raman shift. The Stokes peak was also shown to shift linearly with an applied pure bending stress. Thus in order to evaluate temperature without the influence of thermally induced stresses which may evolve in some MEMS, the ratio of the Stokes to anti-Stokes signal intensities and the linewidth of the Stokes spectral band were calibrated for doped polysilicon over the same temperature range.

Using the calibration data, Raman spectroscopy was implemented for the evaluation of temperature of thermal MEMS with sub-micron spatial resolution. Heated AFM cantilevers and micro-beam heaters were chosen due to their wide range of applications. Different thermal and mechanical boundary conditions were considered by studying both the beams and cantilevers, resulting in varying levels of thermal stress. By using the three calibrations in a complementary fashion for device measurement, the validity of Raman thermometry was explored. Device temperatures of up to 650ºC and their corresponding uncertainties were realized. Effects of thermally induced stress were taken into account and analyzed simultaneously. Comparisons were made between experimental results and FEA modeling.

Parameters that affect the Raman thermometry technique were reported and elucidated. This includes aspects such as laser heating, spatial and spectral resolution, light collection efficiency, measurement uncertainty, and instrumental drift. This in-depth analysis helped to establish the accuracy of Raman thermometry for MEMS.

CHAPTER I

INTRODUCTION

1.1 Motivation for Research

In recent years, research efforts in the design and production of micro and nanoscale devices have outpaced those focused on the ability to accurately determine performance factors. Thermal micro electro mechanical systems (MEMS) are a class of devices that are in need of thermal metrology tools. These devices, when operational, are capable of reaching temperatures in excess of 700-800ºC, and maintaining large temperature gradients across their geometries, whose critical dimensions are on the order of 1-5 μm. Accurate temperature measurements at high spatial resolution across a wide range of temperatures are necessary to assess design reliability and performance of such devices, and verify modeling efforts. Thermal MEMS are a class of structures or devices that require the control of heating to perform their task. This chapter introduces several types of devices in the field of thermal MEMS and their functions, and leads into available thermometry techniques.

Thermal actuators rely on thermal expansion through Joule heating to achieve a range of in-plane deflections and actuation forces. U-shaped cantilevered thermal actuators depend on a varied beam cross-section to produce local heating on one side of the U-shape, causing axial deflection in that region only and bending of the entire structure. This configuration has lead to reports of deflections of 20 μm, depending on the length ratio of the hot and cold legs [1] and actuated forces on the order of 10-20 μN

[2, 3]. Similar electrostatic actuators are capable of producing forces on the same order magnitude as these structures (10 μN) requiring input voltages on the order of 100 V, ten times that required by thermal actuators [4]. Bent beam actuators (similar to Figure 1) utilize thermal leg expansion to cause linear displacement of a center shuttle. Depending on the leg configuration (single or multiple), actuation forces of up to 1-10 mN have been measured with power dissipations of 150-250 mW, reaching temperatures in excess of 500ºC [5, 6]. An order of magnitude less force was found when using a multiple leg scheme, requiring 50-60% less power. Such actuators have been applied to functioning rotary and linear displacement micro-engines [7]. In comparison, the bent-beam design provides forces 2-3 orders of magnitude higher than the U-shape with similar deflections and power dissipation. Similar devices have been fabricated and extensively modeled, both thermally and mechanically [8].

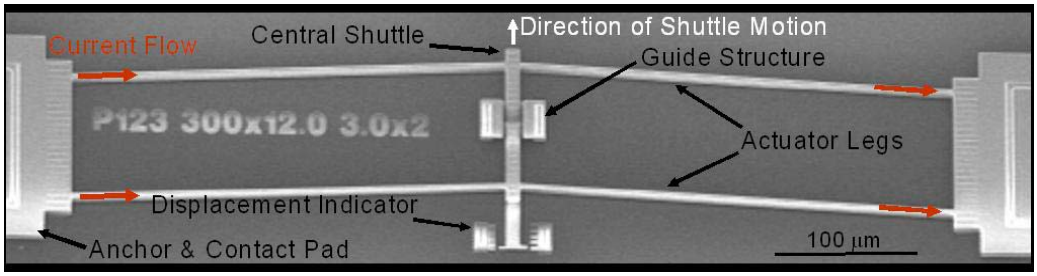

Figure 1. Bent-beam thermal actuator (Courtesy of Sandia National Labs) [6].

Opto-mechanical actuators have also been fabricated from polysilicon (Figure 2), utilizing the heat flux of an incident laser beam to cause thermal expansion. By heating such structures optically, these electrically isolated devices can be used in remote situations [9]. Thermally induced damage has been reported for these actuators when

using high-fluence IR excitation [10]. Since these devices are made from polysilicon films, it is believed that temperatures must exceed 1200ºC in order to observe melting and recrystalization that has been observed in these devices. A need for monitoring the temperature during operation exists for this reason. Actuation produced by thermal expansion has been used for concepts such as micro-switching or gripping devices [11].

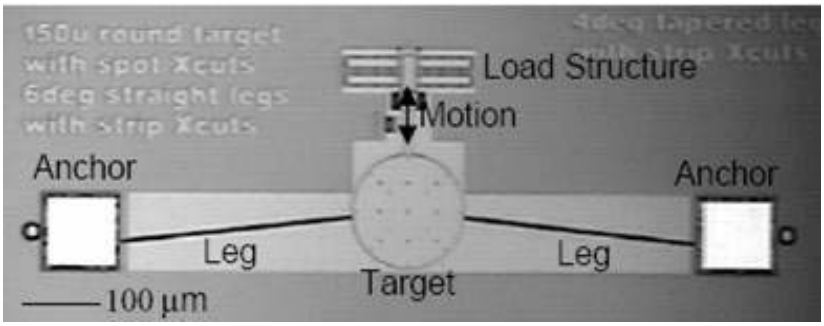

Figure 2. Opto-mechanical thermal actuator [10]. Laser fluence is focused on the center disk in order to cause heating and expansion along the legs of the device. Melting of the center disk has been observed in some cases when high fluence IR lasers are used.

Chemical sensing has been performed using polysilicon micro-hot plates [12, 13]. In order to successfully detect certain gas species, polysilicon heaters (Figure 3) are used to control the sensitivity of metal silicon dioxide membranes for sensing. When the sensing of combustible gases is of interest, thin metal-oxide membranes from materials such as SnO_2 are used, because their resistance decreases upon gaining electrons from the gas [14]. Temperatures greater than 400-500ºC have been predicted and measured for these devices when operational [15]. Heating the membrane can increase reaction rate and response time and is often performed using microfabricated polysilicon heaters. Knowledge of the temperature distribution of these sensors and the thermal response of the polysilicon heater is crucial, as their sensitivity, and thus usefulness is a direct result.

Excessive heating can cause stress issues within the sensing membrane, and create non-uniform temperature distributions, both of which can affect performance. Such sensors are beneficial to industry, where fuel oxidants and propellants are dangerous to human health and the environment.

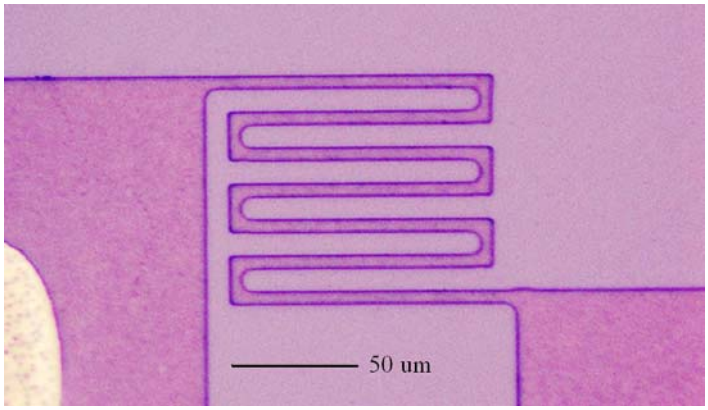

Figure 3. Polysilicon serpentine micro-heater. A potential is placed across the two large contact pads, causing Joule heating in the thin resistive beam. Such a heater can be fabricated below a metal-oxide film for gas detection.

In the field of scanning probe microscopy, heated AFM cantilever probes (Figure 4) are used for thermo-mechanical data storage in thin polymer films [16, 17]. These devices were initially developed at IBM Research Division in Zurich, Switzerland, as part of the Millipede project [17]. An integrated heater in the tip region of an AFM heats the tip, allowing it to write indentations in thin polymer films with nanometer dimensions. The AFM tip can then be used to scan the surface to read the data stored by the indentations. Such advancements have lead to data storage densities of 0.9 Tbit in^{-2}. Device performance and sensitivity are directly related to corresponding thermal and electrical behavior. Thermal Dip Pen Nanolithography (t-DPN) is a patterning technique capable of defining features in the 10-100 nm regimes. A solid organic (melting point:

100ºC) was used to write lines 100 nm in thickness by toggling the AFM heating, and controlling the cantilever's position [18]. This form of nanolithography has also been carried out by thermally actuated probe arrays [19]. At present, these small heat sources are being investigated as thermal AFM probes in order to examine chemical reaction kinetics, induce grain growth, and locally modify materials. In these cases, the AFM probes, made from silicon, may need to reach temperatures up to 900ºC. Accurate knowledge of the electro-thermal behavior of these probes is necessary for the realization of this technology.

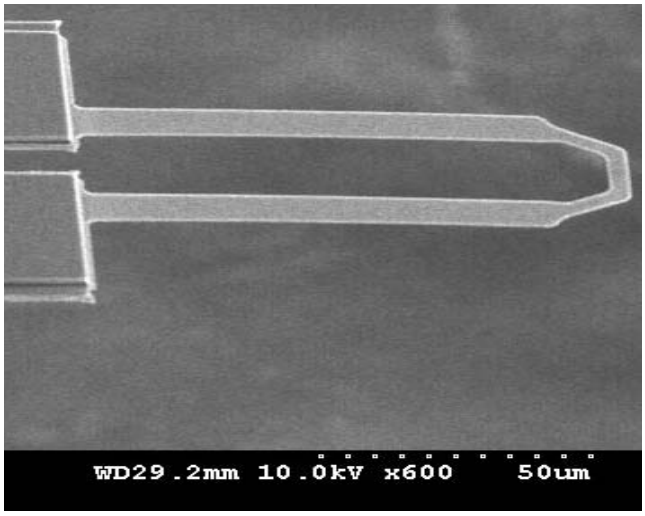

Figure 4. Heated AFM Cantilever [20]. Electric current flows through the legs and heater (end of U-shape) regions. Localized high temperatures are maintained around the probe tip, which is located on the highly resistive heater.

Carbon Nanotubes (CNTs) and nanowires are of great interest in nano-technology due to their excellent thermal and structural properties. High strength composites, AFM probe tips, and chemical and biological sensors are just a few of the possibilities [21]. However, growing these nanostructures locally on the features of larger scale MEMS is

still in developmental stages. The growth of carbon nanotubes and nanowires can be achieved by a chemical vapor deposition (CVD) process at temperatures from 500ºC to 900ºC using various metal catalysts and hydrocarbon gases. The necessary heating for growth can alternatively be provided by polysilicon micro-heaters. This technique has been used for the local growth of CNTs in a room temperature CVD process [22]. Because the type, quality, and size of CNTs is greatly dependant on the growth temperature, temperature mapping of such heated structures in the range of 500ºC to 1100ºC is needed for characterization and localized growth of carbon nano-structures.

Advancements in the field of silicon MEMS micro-engines has lead to improved efficiencies in electrical to mechanical energy conversion and micro-gas turbine applications [23, 24]. These devices, of millimeter dimension, are capable of power production in the 10-100 W range, creating a light-weight, portable energy source. Extremely high rotor speeds are maintained in these devices, with gas turbine inlet temperatures capable of reaching 500-1000ºC during operation [25]. Accurate thermometry of these devices will lead to improved thermodynamic and mechanical functionality, and thus overall output and efficiency.

1.2 Thesis Overview

The purpose of this research is to implement Raman spectroscopy as a robust thermal metrology technique capable of mapping temperature with high accuracy across a broad range of temperatures in thermal MEMS devices. The sub-micron spatial resolution available to this technique can be realized for devices such as the Silicon-based MEMS mentioned in the previous section, which are capable of reaching temperatures of 900ºC. This experimental method is shown to provide accurate temperatures of these

devices with a simple calibration technique in order to evaluate their functionality and reliability. A complete evaluation of the technique, as well as the necessary instrumentation, experimental error, resolution and validity of results by modeling is included.

Chapter 2 presents a survey of the current thermal measurement technology used for these length scales, and focuses on the respective advantages and disadvantages of each method. Raman spectroscopy is introduced, and its theory, instrumentation, previous research, and applications are discussed in chapter 3. Experimental methodologies and sample fabrication are discussed in chapter 4, followed by discussions of calibration techniques and thermometry experimentation of two types of thermal MEMS devices in chapter 5. Chapter 6 compares corresponding experimental and theoretical results of the thermal metrology. Conclusions of the overall study are found in chapter 7, in addition to future directions for this work.

CHAPTER II

BACKGROUND AND LITERATURE REVIEW

The following chapter introduces and reviews some of the thermometry techniques used in semiconductor and micro-device research today. All methods, electrical and optical, have their advantages which are highly dependant on the desired resulting data, material under study, and dimensions of the features. Of the technologies which exist to measure temperature, optical methods are preferred due to their non-destructive nature, high spatial resolution potential, and ability to be accurately calibrated. An excellent and more detailed review of such techniques is provided by Zhang [26]. This review aims to give the reader a general knowledge of the field, and present Raman spectroscopy as an ideal technology for the thermometry of silicon thermal MEMS devices.

2.1 Micro-Infrared Radiation Thermometry

Micro-IR thermometry has proven to be popular in the IC (integrated circuit) industry, due to its accuracy at lower temperature ranges (< 150ºC) [27], and the ability to produce transient and static full-field temperature maps for determination of localized "hot spots". IR detection is made possible through the use of cooled detectors made from compound semiconductors such as InSb (3-5 μm wavelength sensitivity) and HgCdTe (8-12 μm sensitivity) [28]. A typical IR system is calibrated by focusing onto a surface of a known temperature in order to create a spatially varying emissivity map. This calibration can be performed at several temperatures in order to determine the variance in apparent

emissivity with temperature. The emissivity is then assumed to be constant over some range of temperature. An apparent temperature map is then collected of the powered device. The apparent temperature map and the emissivity map are aligned, and the corrected temperature map is found based on the estimated temperature dependence of the emissivity.

The minimum focused spot diameter of the IR-microscope is the lower limit of spatial resolution. This diameter, d_o, is the far-field diffraction limit, which is a function of both the radiation wavelength (λ_i) and the numerical aperture (NA) of the microscope objective (equation (2.1)).

$$d_0 = \frac{\lambda_i}{2NA} \tag{2.1}$$

Therefore, spatial resolution is directly related to the range of wavelengths to which the detector is sensitive. By using InSb detection, length scales of 1.5-3 μm could be resolved theoretically, but are often not realized [29, 30]. This resolution of far field micro-IR systems is not adequate for analyzing structures such as the heated AFM probe (Figure 4), as seen in Figure 5. Correct surface emissivity values over a broad range of temperatures are necessary for accurate results. This optical property is dependant on temperature and radiation wavelength. At temperatures below 600ºC, emissivity of bulk silicon varies between 0.1-0.6 for wavelengths of 1-10 μm [26, 31]. Silicon is semi-transparent over the same temperature range for wavelengths greater than 1.1 μm, causing additional measurement uncertainties. Large variations in the optical emissivity occur at smaller wavelengths (1-4 μm), making absolute temperature measurements using detectors of high spatial resolution less effective for thermal MEMS [32].

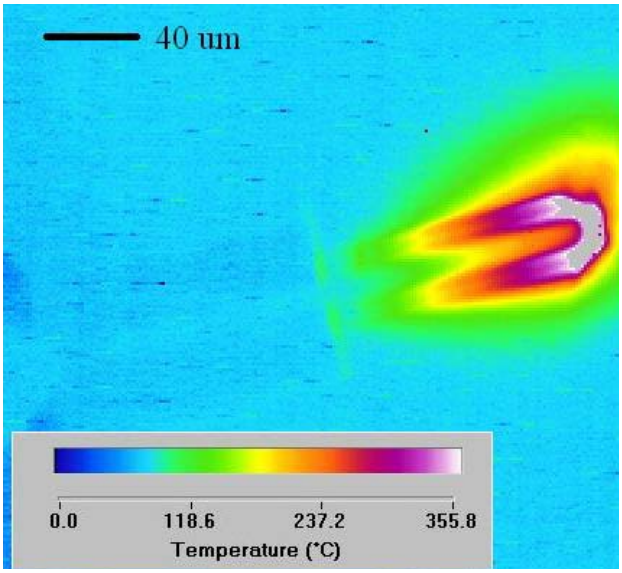

Figure 5. Full field IR temperature image of a Heated AFM Cantilever, as shown in Figure 4.

The use of micro-IR thermography as a transient analysis technique has also been used effectively. Temporal resolutions on the order of 1 μs have been resolved, allowing high resolution transient response analysis [33]. Additional novel studies on IR absorption have been made. Through the use of a solid immersion lens, this imaging technique was shown to have submicron spatial resolution [34, 35], however, low signal to noise ratios and material calibration issues are still present. Another study utilized this absorption technique through an array of bi-material micro-cantilevers. Beam deflection occurred based on the amount of energy absorbed, yielding accuracies of 3-5ºC [36].

2.2 Thermoreflectance Thermometry

Thermal response analysis using thermoreflectance is based on the calibration of surface temperature to the small changes in the optical reflectance of a material due to temperature. A change in temperature, ΔT, can be related to the change in the surface reflectivity, ΔR, by κ, the thermoreflectance coefficient, as shown in equation (2.2) [37].

$$\Delta T = \left(\frac{1}{R} \frac{\partial R}{\partial T} \right)^{-1} \frac{\Delta R}{R} = \kappa^{-1} \frac{\Delta R}{R} \tag{2.2}$$

For materials, this relationship is linear only over a certain temperature range, and the value of κ is wavelength-dependant. This coefficient may be found for a material by calibrating the reflectivity change ratio against a sample of known temperature.

The thermometry measurement using this technique is versatile, and has been used for both ultra-fast time resolution and full-field imaging. During the thermometry measurement, an incident light source (continuous or pulsed laser, LED, white light) on the surface is required. To calculate the reflectivity change, light intensity is measured before and after the powering of a device using photodiodes, photomultiplier tubes, or a CCD (charge coupled device) [37]. Because the reflected signal is weak, experimental modulation along with lock-in detection can be used to reduce noise for a point measurement. Either the frequency of a mechanically chopped continuous laser, pulsed laser, or cyclic sample heating can be used for lock-in amplification. Because this technique allows the use of visible wavelength lasers, sub-micron spatial resolutions can be achieved for thermometry of thermal MEMS devices (equation (2.1)).

This technique is particularly useful for improving the transient aspect of a point measurement. Temporal resolutions in the picosecond [38] and nanosecond regime [39, 40] have been achieved. Using a pulsed laser with a pump-probe experimental scheme, thermoreflectance has been used to measure thermal conductivity, by monitoring heat propagation though solids at nanoscale dimensions [38]. Area-wide imaging is limited by scanning techniques in these cases. As a point measurement, the technique can improve upon transient analysis as compared to micro-IR as well as spatial resolution.

Full-field temperature plots of functioning devices are desired for thermal MEMS, and have been achieved by incorporating CCD detection with thermoreflectance [41]. Full field relative temperature images of polysilicon resistive heaters have been attained using this variation with LED illumination [42]. The capability of 10 mK temperature resolution was shown by mapping a 2-D thermal image using a form of this technique. However, necessary measurement times were on the order of hours, making it a less attractive variation [37]. In general, the dynamic range of an array detector (CCD) is less than that of a point detector (photodiode) and thus integration time is needed.

Absolute thermometry is not practically possible with this method, as a reference reflectivity change for measurements of devices made from thin films are challenging. Factors such as surface interference, device thermal expansion, and surface roughness can greatly impede accuracy over a range of temperatures [43]. Reflectivity measurements on metal films are attainable with this technique; making it attractive to devices with such coatings. Relative reflectivity measurements with picosecond temporal resolution have been attained from thin gold films [44]. Additional advantages of thermoreflectance as a thermometry technique include a wide range of implementation costs, depending on the type of measurement.

2.3 Scanning Thermal Microscopy

Scanning thermal microscopy (SThM) is a contact thermometry technique which utilizes the mechanisms behind atomic force microscopy (AFM) and scanning tunneling microscopy (STM) [38]. These methods are widely known for their application to microscopic surfaces, where data is collected by measuring deflection of a cantilever probe (Figure 6). SThM utilizes a temperature sensor fabricated at the tip of the AFM

cantilever that is held in contact to a surface and scanned over it. Temperature variation may then be mapped over the scanned region. Subsequently, the spatial resolution is determined by the tip radius, or more accurately, by the area of the tip that actually contacts the surface of the sample. This resolution has been reported between 30-50 nm, which is far less than that available with optical techniques [38, 45].

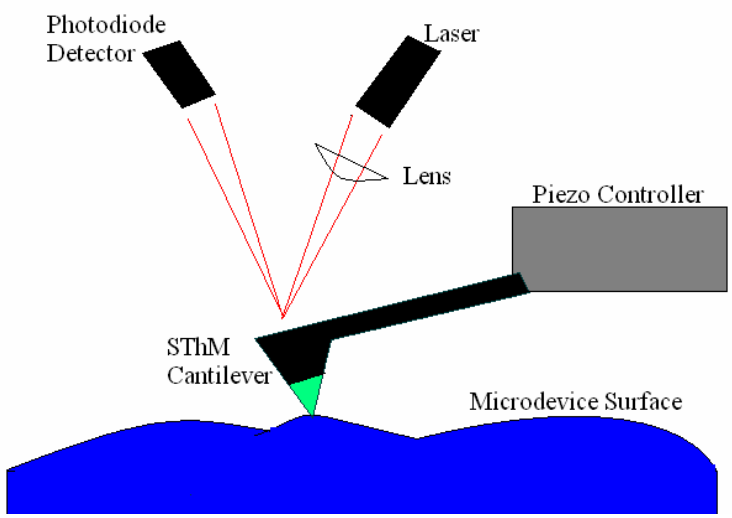

Figure 6. SThM cantilever configuration with integrated thermocouple inside tip. High spatial resolution, which is limited by the AFM tip radius, can be resolved for thermometry and topography measurements.

Scanning joule expansion microscopy (SJEM), is a hybrid of SThM with the ability of relative thermometry for determining localized heating in devices [46]. By applying an AC current to an electrically conductive device, it will periodically heat due to Joule heating at twice the frequency of the current and consequently expand and relax. Using lock-in detection, spatial resolutions of 10-20 nm have been achieved for relative thermometry [47].

The aforementioned scanning probe techniques have demonstrated spatial resolutions at much smaller length scales than optical methods, yet the necessary calibration techniques aren't readily available [26]. Due to the sub-micron (<100nm) dimension of the SThM tip, hysteresis can occur when contacting the probe to the surface due to solid-liquid tension forces [45]. The liquid meniscus creates a thermal resistance between the probe and surface, making absolute thermometry challenging [48]. In addition, the thermal resistances between the tip and air must also be taken into account. Temperature distribution mapping is possible with the technique, yet it is limited to steady state as scanning the probe tip over an entire surface can not be done in times suitable for transient analysis.

2.4 Additional Thermometry Techniques

Several additional optical methods for determining temperature at small scales are currently receiving attention in the field. Fluorescence thermometry is based on the fact that emitted photons from a surface can reach higher energy states. The time required for these fluorescent photons to return to their original energy state, called the relaxation or decay time of the photons, is a function of temperature. A more novel method, fluorescence thermometry has been used to accommodate a wide range of temperature applications [49]. Micro-Fluorescent thermal imaging was used on bio-sensing devices to accurately resolve temperatures up to 50ºC with 0.1ºC accuracy [50]. Complicated experimental setup and many sources of possible error are some disadvantages [51].

Laser interferometry thermography is based on the interference which occurs when light is reflected/transmitted from the top and bottom of the surface film. Typically an infrared wavelength is used as an excitation source, and a detector records both the

transmitted and reflected light. This technique is based on the fact that as the temperature of the sample is increased by a given amount, the optical refractive index changes due to interference. This technique was used as a thermal metrology technique to evaluate both strain and temperature of polysilicon micro-beams above temperatures of 500ºC [52].

2.5 Raman Spectroscopy

Raman spectroscopy is an optical measurement technique that is well suited for the temperature measurements in MEMS devices, especially those made from silicon, due to its strong scattering cross-section. In using a visible light source to initiate the light scattering process, the Raman technique provides spatial resolutions on the order of 1μm or smaller, considering far field diffraction limited optics. Most measurements require photon collection times on the order of seconds, thus this technique is generally applied in steady state temperature mapping. Raman scattering has been used to determine the temperature distribution with micron spatial resolution in silicon and polysilicon devices, diamond structures, and III-V semiconductors [53-61].

The scattering technique has been used in a similar manner to estimate residual stress in released polysilicon beams and cantilevers, stress gradients in as-deposited polysilicon thin films, and microstructural analysis films, both doped and undoped [61-64]. In contrast to micro-IR and thermoreflectance, Raman spectroscopy has been used to yield absolute temperature measurements in micro-devices with submicron resolution. Due to lack of technologies for scanning the absolute temperature of devices between the sub-100 nm regime (scanning thermal microscopy techniques) and 2 μm (micro-IR techniques), Raman spectroscopy has emerged as a potential candidate to address this area for silicon thermal MEMS. The technique is reviewed in depth in the next chapter.

CHAPTER III

RAMAN SPECTROSCOPY

C. V. Raman discovered the optical phenomena in 1928 that would later be named Raman light scattering [65]. By monitoring light scattering from various crystalline and amorphous solids, fluids, and gases with a mercury arc lamp, he was successful in distinguishing elastic light scattering from additional spectral bands. He described this finding as a "spectrum of the new radiation", and deemed it the result of energy exchange between the incident light and scattering medium.

The introduction of the laser in the 1960s allowed Raman spectroscopy to be more accessible to the scientific community. However, the instrumentation, optics, and signal detection developed at a relatively slow pace, most likely due to the weak Raman signal. A strong technological push from the 1980s through the mid 1990s paved the way for the research possibilities of today's Raman spectrometers [66].

This chapter introduces the theory behind Raman light scattering, and the hardware necessary to accurately measure a Raman signature. The focus of this section is to explain the ability of this technique to perform micron spatial resolution temperature and stress mapping in terms of its theory and equipment.

3.1 Theory of Raman Scattering

Raman spectroscopy is an optical chemical analysis technique that measures the intensity of inelastically scattered light over a range of frequencies. During the Raman scattering process, a small portion of the incident photons (1 in 10^6-10^7) are scattered

inelastically due to their interaction with the vibrations or rotations of atoms or molecules. The inelastic exchange occurs because the photons either lose or gain energy from the material under examination. In the case of the solid state lattice of silicon, the photons scatter due to their interaction with lattice vibrations (phonons). The inelastic scattering is a result of a red frequency shift of the scattered photon to longer wavelengths (Stokes shift) or shorter wavelengths (blue, anti-Stokes shift) [26]. In the case of the Stokes shift, an incident photon at frequency ν_i loses energy to the lattice from which it is scattered (ν_i-ν_j), while a photon gains energy from the lattice during the anti-Stokes instance (ν_i+ν_j), (Figure 7).

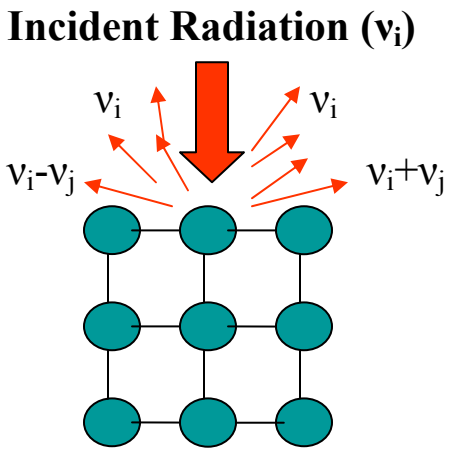

Figure 7. Visualization of Raman light scattering from a crystal lattice

3.1.1 Raman Scattering Physics

By collecting the scattered photons of inelastic scattered light across a range of frequencies, Raman is a powerful chemical analysis technique for monitoring phonon resonances. The following derivation is based on classical electromagnetic theory, and

aids in the understanding of theory of Raman and Rayleigh scattering theory [67]. Incident radiation on a Raman-active atom creates an oscillating induced electric dipole moment, *P,* throughout the electron cloud surrounding the atom (Figure 8). The dipole is proportionally related to the electric field of incident light, E_i, by the polarizability α, of the bonds in the medium (Equation (3.1)). This bond polarization is essentially a measurement of how readily a dipole moment is induced in the atom. The incident electric field is a function of its frequency, ν_i, and magnitude, E_0, (Equation (3.2)).

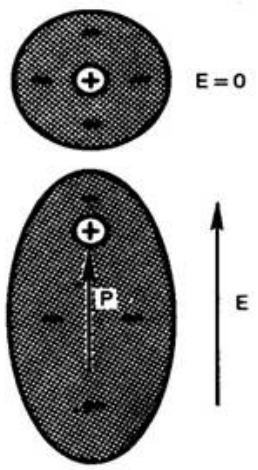

Figure 8. Visualization of an induced dipole moment before and after an electric field is applied to an atom [68].

$$E_s \propto P = \alpha E_i \tag{3.1}$$

$$E_i = E_0 \cos(2\pi \nu_i t) \tag{3.2}$$

The dipole moment vector P is actually the sum of the first order term (shown above) and higher order terms, though only the first order term is shown due to the fast-converging series. To account for the fact that the atoms in a solid state lattice are

constantly vibrating in and out of their equilibrium position, the polarizability term may be expanded in a Taylor Series.

$$\alpha = \alpha_0 + \left(\frac{\partial \alpha}{\partial Q_j} \right) Q_j + \ldots \tag{3.3}$$

Here, Q_j are the normal vibrational modes of the lattice. Assuming harmonic motion, the lattice vibrates at a certain phonon frequency:

$$Q_j = Q_j^0 \cos(2\pi \nu_j t) \tag{3.4}$$

Where ν_j is the frequency of the j^{th} vibrational mode. Thus, by combining equations (3.1)-(3.4), the scattered light field can be found with the first two terms of the polarizability expansion:

$$E_s = \alpha_0 E_0 \cos(2\pi \nu_i t) + E_0 Q_j^0 \frac{\partial \alpha}{\partial Q_j} \left(\frac{\cos(2\pi(\nu_i + \nu_j))t + \cos(2\pi(\nu_i - \nu_j))t}{2} \right) \tag{3.5}$$

Equation (3.5) shows a classical mathematical representation of both Rayleigh and Raman scattering. The electric field of the scattered light, E_s, is a sum of three terms. The first term is oscillating at the same frequency as the incident radiation. This instance is known as the Rayleigh, or elastic scattering. A photon that experiences this type of scattering has no net change in energy, following Planck's Law. The remaining two cosine terms are evident of Raman scattering. This is the result of the incident light frequency coupling with that of the first Raman resonance mode of a lattice. The first of the two terms is the anti-Stokes shift, while the 2^{nd} term is the Stokes term.

Figure 9 is a typical Raman spectrum of silicon at room temperature. The horizontal axis represents the frequency shift of scattered photons relative to their incident (Rayleigh) frequency, conveniently expressed as the Raman shift. The unit is

the wavenumber (cm^{-1}), which is simply the oscillating frequency divided by the speed of light, *c*. The vertical axis shows the amount of counts occurring at each of the Raman shifted frequencies. The Stokes Shift of room temperature Si is found at or near 520.5 cm^{-1}, while the anti-Stokes is exactly mirrored about the Rayleigh scattering frequency at -520.5 cm^{-1}.

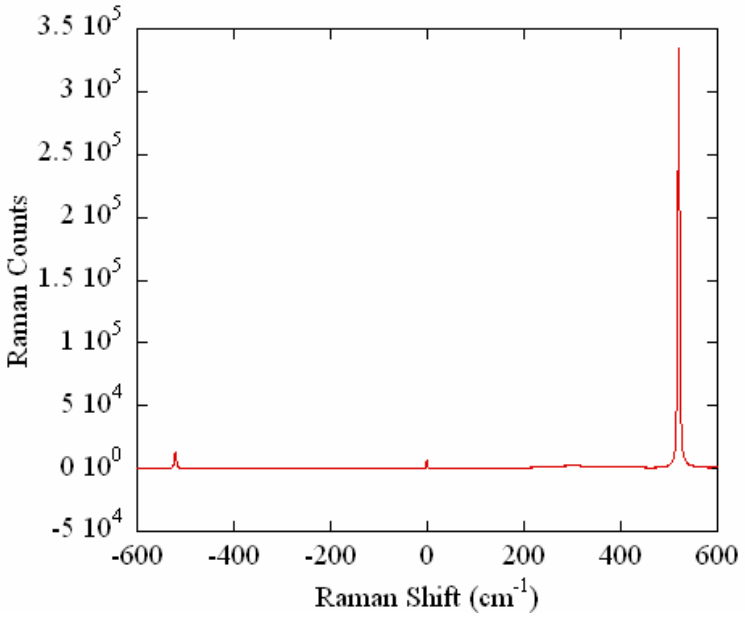

Figure 9. Full spectrum of the first Raman transition of single crystal silicon at room temperature. The Stokes signal (right) is over an order of magnitude greater than the Anti-Stokes signal (left). A filtered Rayleigh signal is seen at 0 cm^{-1}.

In summary, the frequency of the first phonon resonance (represented by the Stokes and anti-Stokes Raman shifts) is directly related to the bond polarization of a lattice, which is in turn a function of interatomic potentials. Figure 8 gives additional insight to this phenomenon, as it shows a change in dipole moment effects the resultant scattered electric field. Since the frequency shift centers on that of the incident photon, only low frequency optical phonons near the dispersion zone center take part in the

Raman scattering. Thus, any effect which alters the lattice spacing (e.g., expansion or contraction due to stress and/or thermal loadings) will result in changes of the frequency where the first Raman phonon mode occurs. A Raman active material is one in which dipole moments can be induced, thus Raman scattering has been used in the diagnostics of solids, liquids and gases. Metals are not are not measurable using Raman spectroscopy due to their free electrons which prevent induced dipole moments.

3.1.2 Implementation of Techniques

In order to accurately implement Raman spectroscopy for thermometry applications, a relationship between sample temperature and the effect on its Raman signature must be established which ideally would be purely temperature dependant. However, it is known that mechanical stress can affect certain aspects of the Raman response. In order to measure temperature, any effects of evolving stress due to thermal loading must be understood and accounted for, if they are significant. Based on previous research on Si, it is known that increasing temperature or tensile stress (lattice expansion) will shift the Stokes peak towards lower frequencies and may be approximated as a linear shift over a wide range of temperatures or stresses [69-71]. In addition, increasing temperature of the lattice results in an increase of the Stokes full width at half maximum (FWHM), or linewidth. The linewidth, in cm^{-1}, is defined by the width across the Stokes peak at half of the total measured counts. The broadening of linewidth with temperature is due to increased phonon relaxation rates.

The linear coefficients of peak shift associated with temperature and stress have shown a wide range of variation for polycrystalline silicon in the literature, and its source is not well understood. The monitoring of the Stokes linewidth as a function of

temperature has received less attention; one study of interest measured temperature in diamond using the calibration, correcting for instrument linewidth [72]. The effect of stress on the Raman peak position in polysilicon has been found to be between -2.1 and -4 cm^{-1}/GPa [73, 74] and for temperature -0.021 to -0.02299 cm^{-1}/ºC [55, 69]. In one study, temperature was calibrated using the Stokes shift to 600ºC, and used to measure polysilicon micro-bridges with accuracies of ±20ºC [69]. Kuball et. al. used this calibration technique to analyze AlGaN/GaN HFETs with an accuracy of 10ºC, extending the technique to non-silicon semiconducting materials [59, 75]. The possible effect of thermally induced stress was not accounted for in all these temperature measurements studies.

It is possible to monitor the temperature of a crystal lattice through the ratio of the Stokes to anti-Stokes intensities (a measure of peak signal counts or spectral area). The Stokes/anti-Stokes intensity ratio method is a well established thermometry technique and is extremely powerful because this ratio directly depends on the Bose-Einstein equilibrium phonon distribution of the lattice, a sole function of temperature. As temperature increases, the number of thermally excited phonons at a given frequency increases, thus the probability that a photon will gain energy from interaction with a phonon increases. Therefore, the anti-Stokes signal will increase with temperature, while the Stokes will decrease. Following this theory, the ratio of the two peak counts decays exponentially with temperature, as seen in Equation (3.6) [76]:

$$\frac{I_{Stokes}}{I_{Anti-Stokes}} = \frac{\alpha_i + \alpha_{AS}}{\alpha_i + \alpha_S}\left(\frac{\omega_i - \omega_l}{\omega_i + \omega_l}\right)^4 \exp\left(\frac{\hbar\omega_l}{kT}\right) \tag{3.6}$$

Here, $\hbar$ is Planck's constant divided by 2π, k is the Boltzmann constant, T is the absolute temperature of the sample, and α is the absorptivity of the material at the incident, Stokes, and anti-Stokes frequencies. Theoretically, the ratio decays exponentially to unity as T approaches infinity. It is important to note that although the intensity ratio is dependant upon the optical absorption and Raman scattering cross section of the material under investigation, its intensity ratio may be calibrated with temperature and fitted exponentially.

Temperature in diamond was measured to 1850K using the intensity ratio and peak position calibrations [77]. Additionally, measurements on III-V materials such as GaAs have been reported using the intensity ratio [57]. In another study, both temperature correlations were used for similar materials, however the comparison was made on devices maintaining temperatures below 200ºC [58]. Temperatures were resolved for a laser heated silicon AFM cantilever via intensity ratio, and used for model verification [78].

Solid state modeling has been used to calculate the Raman Stokes position and linewidth over a broader range of temperatures (5-1400K) of single crystal silicon [76]. Greater precision in determining the temperature of pure crystals over this range of temperatures may be obtained through three and four phonon process modeling using Equations (3.7) and (3.8), respectively. Here ω_0, A, B, C and D and are material specific parameters, ω is the Stokes frequency, and Γ is the Stokes linewidth. A linear assumption for calibrations is highly accurate between room temperature and 1200K [79], providing constant calibration sensitivity across its range. This assumption does not hold across temperature extremes, as seen by the following equations.

$$\omega(T) = \omega_0 + A\left(1 + \frac{2}{e^{\frac{\hbar\omega_o}{2kT}} - 1}\right) + B\left(1 + \frac{3}{e^{\frac{\hbar\omega_o}{3kT}} - 1} + \frac{3}{(e^{\frac{\hbar\omega_o}{3kT}} - 1)^2}\right) \tag{3.7}$$

$$\Gamma(T) = C\left(1 + \frac{2}{e^{\frac{\hbar\omega_o}{2kT}} - 1}\right) + D\left(1 + \frac{3}{e^{\frac{\hbar\omega_o}{3kT}} - 1} + \frac{3}{(e^{\frac{\hbar\omega_o}{3kT}} - 1)^2}\right) \tag{3.8}$$

While the intensity ratio method may be used to find temperature based on classical mechanics, this ratio approaches a constant at elevated temperatures (above 500ºC for silicon), causing the sensitivity to dramatically decrease at high temperatures. Effects such as thermal stresses which can evolve during heating will not affect the measurements made using the ratio, as it is a sole function of temperature. However, this method is difficult to calibrate and is highly instrument dependant. In addition, extended collection times are necessary in order to resolve the weak anti-Stokes signal. At room temperature, the anti-Stokes peak signal is roughly 20x weaker than the Stokes, while at temperatures in excess of 750ºC, the Stokes is greater by only a factor of 3 to 4. Thus, mapping device temperature at lower temperatures (< 400ºC) using the intensity ratio may require excessively long measurement times.

Several studies investigating microstrucural characteristics and residual stress in silicon structures using micro-Raman spectroscopy have been published. Film thickness profiling of poly-Si was done by varying the excitation laser wavelength, and thus the optical penetration depth, to probe various film depths [32, 80, 81]. This type of study allowed the shape of Raman spectra to be correlated to various grain structures and verified by microscopy. A more in-depth study of microstructural parameter fitting has been performed on polysilicon, indicating nanostructured materials cause an additional asymmetry in the Raman signature due to phonon confinement [54]. In general, these

effects can alter the Raman shape (linewidth), but will not affect the peak frequency, which is an additional advantage of the calibration.

Hydrostatic residual stress in polysilicon micro-beams was quantified effectively using the linear Stokes Raman shift [63, 71]. The technique was found useful over a range of processing conditions such as dopant uniformity and diffusion anneal. Finite element analysis was used accurately to verify experimental residual stresses determined by Raman mapping of simple micro-beams [64]. Both stress and temperature were scanned independently using the phonon frequency shift of polysilicon, by making use of a line focused objective to simultaneously collect multiple spectra [61]. Of the surveyed literature, there has currently been no emphasis placed on induced stresses caused by the heating of powered silicon thermal MEMS devices, and their effect on thermometry measurements using Raman.

In summary, there are issues which have not been addressed when using Raman for micro-thermometry. The research provided by this study consists of a full analysis of the Raman technique for measuring temperature and accounting for stress in simple silicon and polysilicon structures using frequency shift, linewidth, and intensity ratio. By following a complementary use of these methods to examine microdevices, as well as accuracies, reproducibilities, and instrument parameters, a well established thermal metrology technique is realized from Raman spectroscopy.

3.2 Micro-Raman System Hardware

The equipment used to acquire Raman signal data has evolved over the past decades to accommodate the growing applications of Raman spectroscopy. Raman systems are designed with the necessary equipment to obtain fast, high signal to noise

ratio (SNR) spectra, with high accuracy and efficiency. A typical micro-Raman system consists of a microscope and stage, excitation laser, filters, slit, diffraction grating, necessary optics, detector, and post-processing software (Figure 10).

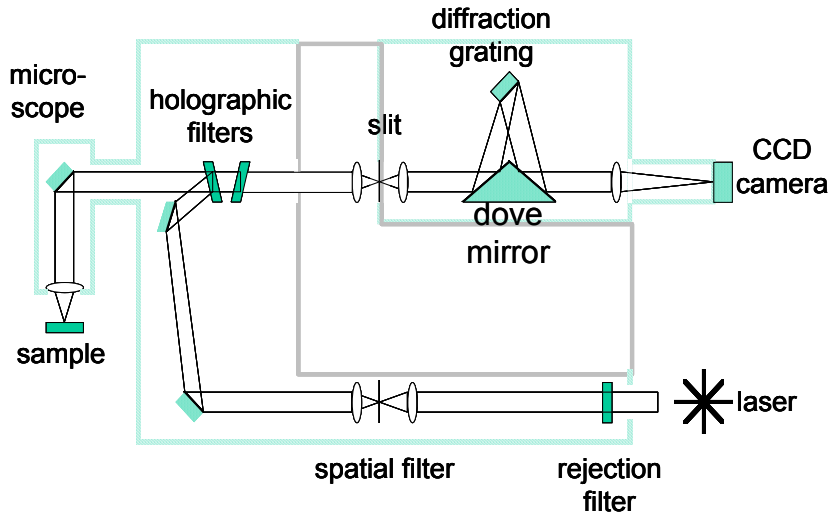

Figure 10. Typical Components of a multi-channel dispersive micro-Raman System (Renishaw Inc.). A collimated beam is focused on the sample. Scattered light is directed through the optics of the spectrometer, and measured by the CCD.

A dispersive Raman system is an obvious choice for semiconducting materials such as silicon. This type of system, when making use of array detection for photon collection and excitation wavelengths in the blue-green regime, takes full advantage of the strong scattering cross-section of silicon. A CCD detector is an array of pixels on a Si integrated circuit. Its quantum efficiency, (ability to convert photons to photoelectrons), provides excellent SNR, and allows the use of lower laser powers with reasonable collection times. There is a spectral range/resolution trade-off, as the CCD is finite in size. However this is not an issue in this study, as the silicon first phonon resonance is located within a range of 25 cm^{-1}, depending on sample temperature and/or stress.

By using visible or ultra-violet lasers, sub-micron diameter spot sizes may be focused on the sample. The corresponding depth of laser penetration, δ, is dependant upon the absorption properties, α, of the polysilicon film at a particular wavelength. As shown in Equation (3.9), the extinction coefficient, κ, may also be used for the calculation.

$$\delta = \frac{1}{\alpha} = \frac{\lambda_i}{4\pi\kappa} \tag{3.9}$$

Absorption coefficients of 2.08E4 and 1.48E4 cm^{-1} at wavelengths of 488 and 514 nm, respectively, were used to determine δ for undoped polysilicon [82]. Optical penetration of these wavelengths was determined as 481 and 657 nm, based on the above relationship. These values are slightly less than that of bulk silicon (0.5μm for 488nm and 0.75μm for 514nm) [83], as expected from the grain structure. The spectrum attained from this spot size is not a true surface measurement, but is actually averaged over all crystal faces seen throughout the entire optical penetration depth of the excitation beam. Therefore, the spectrometer accumulates scattered photon counts from the entire depth seen. A more accurate surface thermometry could possibly be performed using shorter wavelengths (smaller penetration depth). In general, through thickness temperature variations are expected to be small, thus averaging over the depth of the film should not be an issue. Fluorescence is a phenomenon that is more likely to occur using higher energy photons (near-UV and UV wavelengths), and can often hide various aspects of Raman signatures, depending on the material.

Monochromatic light, generated by the laser cavity, enters the system where its power is governed by neutral density (ND) filters. The power provided by the laser is directly related to the peak counts and signal to noise (SNR) ratio of the Raman peaks.

The beam then passes through a spatial filter, which removes any higher order spatial modes so that the beam achieves a better focus. The light is directed to the microscope and focused by the objective on the sample. Scattered radiation from the sample is then collected by the objective and directed to the spectrometer. Elastically scattered light is filtered from the scattered radiation by the holographic (notch) filter. This component is extremely important, as Rayleigh scattering dominates the Raman signal.

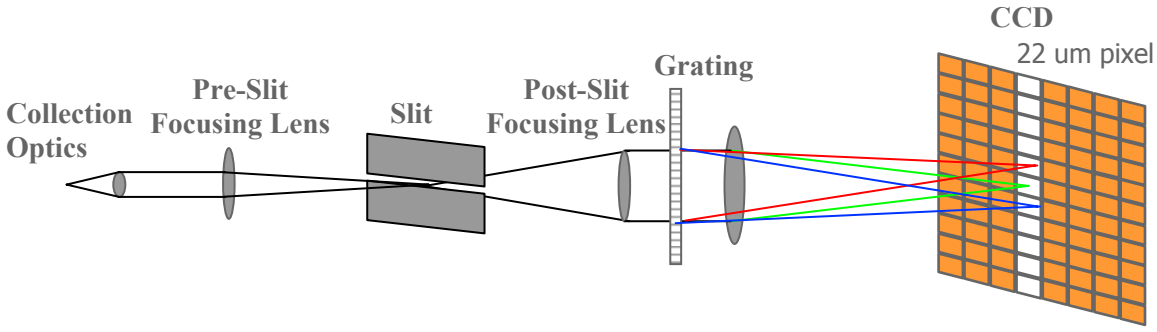

Figure 11. Dispersive multi-channel spectrometer details (Renishaw, Inc.). Optical components are optimized for spectral intensity and resolution.

Following the notch filter the beam of Raman light enters the spectrometer (details in Figure 11). A pre-slit lens focuses the image on the adjustable slit, which dictates the spectral resolution of the system. A post-slit lens then collimates the incoherent Raman signal, which is then focused on the CCD after being separated by the diffraction grating into discrete wavelengths, where each frequency is measured simultaneously. Assuming a static scan is made, only a finite range of wavelengths reach the CCD via the diffraction grating. The adjustment of the slit has a direct impact on the spectral resolution of a Raman spectrometer (product of the slit width and the dispersion), as the focused image on the CCD can be proportional to its width. As the slit width

decreases, the size of the focused image on the CCD camera decreases. Therefore, the ratio of the linewidth of the Raman band to the corresponding amount of pixels exposed after separation into individual wavelengths by the grating decreases, improving spectral resolution.

Photoelectrons are created in the CCD upon exposure to the scattered beam. The dispersed beam is spread vertically across horizontal lines of pixels, which are binned, or summed, to integrate each signal. Raman counts are based on the analog to digital conversion from the amount of photoelectrons at each wavelength, to an electric charge. This electric signal is then processed by the integrated system software. By isolating the CCD area where the beam is focused, any possible stray light directed at the detector can be removed.

As with any backscattering geometry, a trade-off between signal intensity and spectral resolution exists with Raman spectroscopy. Decreasing the slit impedes the signal reaching the detector, yet does improve the resolution. In addition, an increased spectrometer focal length yields better spectral dispersion, because greater length allows the separated wavelengths to spread further apart, disperse over a larger area of the CCD, causing less frequency shift per pixel. This in turn means the same amount of signal is spread over a larger detector area, and longer integration times are required to collect comparable signals. This is especially true for triple stage spectrometers which have the highest spectral resolution, but are known to require long integration times. A shorter focal length will have an increased Raman signal, because it has the same amount of signal spread over a smaller area of the CCD than a longer focal length system, giving it a larger signal per pixel.

CHAPTER IV

EXPERIMENTAL METHODS AND DEVICE FABRICATION

The following chapter outlines the initial characterization procedures for implementing Raman spectroscopy as a thermal metrology technique. Three dispersive Raman instruments were used in this Study: two Renishaw InVia microscopes (Georgia Institute of Technology, Atlanta, GA and Sandia National Laboratories, Albuquerque, NM) and a JY Dilor XY800 (Oak Ridge National Laboratories, Oak Ridge, TN). In the first section, various measurement issues are addressed in depth on both Renishaw instruments, such as laser induced heating, resolution, signal efficiency, and instrument uncertainty. The majority of the data was taken on these two instruments. The second section outlines the processes used for the polysilicon growth and fabrication of the micro-devices used in this study.

4.1 Initial Evaluation of the Renishaw micro-Raman Systems

The majority of the experimentation in this study was performed using the Renishaw InVia Raman microscopes at Georgia Tech (GT, shown in Figure 12) and Sandia National Labs (SNL). This section presents an evaluation of sample laser heating, spatial and spectral resolution, photon counting efficiency, uncertainty, and instrument drift. These are issues that should be addressed for a particular system in order to assess the accuracy and uncertainty of Raman temperature measurements. A deeper understanding of the measurement and equipment is essential in improving the effectiveness of Raman spectroscopy as a thermometry technique for Si-based MEMS.

The systems were operated in 180º backscattering geometry, with an excitation laser line of 488 nm produced by an Ar+ laser. Both were optimized for high spatial and spectral resolution measurements of semiconducting materials by utilizing two different 50X objectives (NA: 0.55, 0.75), a grating of 3000 lines/mm in minus one order (grating orientation), and a spectrometer focal length of 250 mm. A Pryor XYZ translational stage provided sample positioning with 0.1 μm accuracy for the mapping of small features. Aside from its additional automation, the Renishaw micro-Raman system used at SNL is nearly identical to the GT system in regards to laser line, optics, and spectrometer specifications.

Figure 12. The Renishaw Raman microscope at Georgia Tech.

4.1.1 Sample Laser Heating

Laser power may be sourced from 10-25 mW, and adjusted in 0.1 mW increments. This is not the laser power exposed on the sample, due to optical losses throughout the beam path, and the ND filter setting. A Newport 8400 optical power

meter with 818ST detector (Wavelength range: 400-1100 nm; Power range: nW-W) was used to measure the actual laser power where it is incident upon the sample. The ND system filter may be set to 100%, which passes all of the sourced power minus intrinsic optical losses from stationary optics in the beam path, or can be attenuated to 50%, 10%, 5%, 1%, 0.5%, 0.1% etc. Sample laser power was measured at each discrete filter percentage from 100% down to 0.5% for sourced laser powers of 10, 15, 20, and 25mW, using both the 50X and 50X LWD (long working distance) objectives (Figure 13).

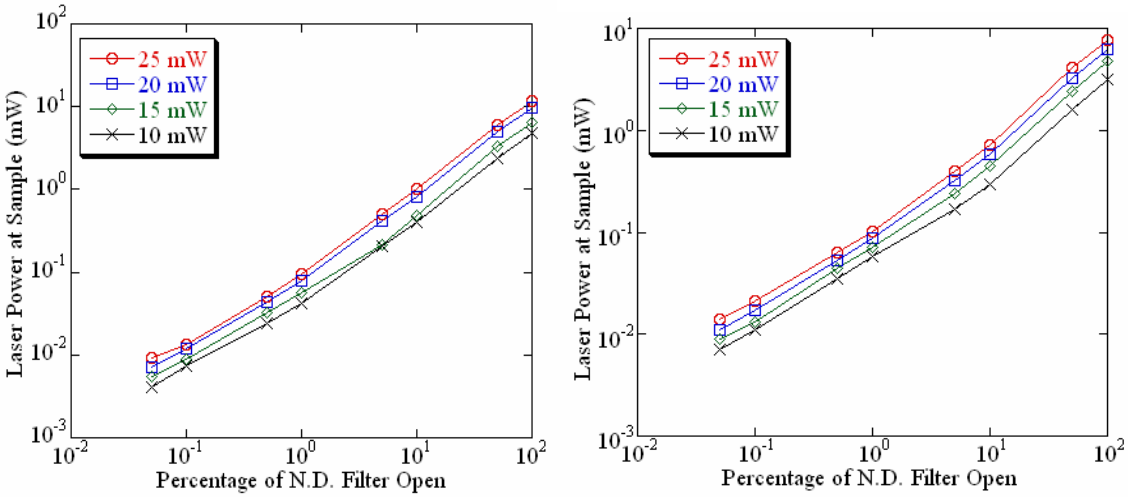

Figure 13. Measured laser power at the sample, as a function of N.D. filter percentage. The amount of laser power at the sample is nearly linearly related to that which is sourced (average R^2=0.9994): Left) 50X objective, Right) 50X LWD objective.

While Raman thermometry is an optical technique which requires no physical contact with the surface of the specimen, this technique can be sensitive to errors caused by sample heating from the probe laser. Sample heating becomes very problematic for devices with small thermal masses. Such devices are often encountered in MEMS devices in the form of small structures and/or suspended devices (e.g., cantilevers, beams,

etc.). Thus, it is quite possible for the focused laser to cause additional heating in many common surface micromachined MEMS devices, which can cause substantial error in the corresponding thermometry.

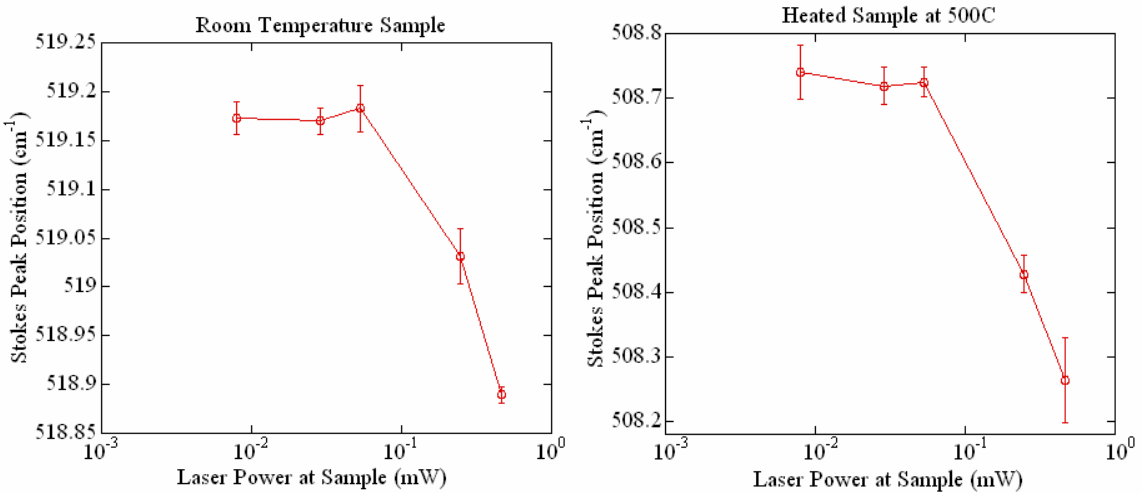

Figure 14. Laser heating does not effect the Stokes peak position of a polysilicon micro-beam with sample laser powers below 50 µW. Measurements were made on a micro-beam at: room temperature (Left), and 500ºC (Right).

Figure 14 demonstrates the significance of laser heating effect on the measurement of a polysilicon device at room temperature and 500ºC. For this experiment, the probe laser was focused on the center of a 300 x 10 µm heavily doped polysilicon beam. By simply exposing a room temperature sample to varying laser powers at 488 nm, the Stokes peak position shifts nearly 0.3 cm^{-1} (increase in temperature). An increase in the peak shift (0.5 cm^{-1}) is seen when comparing the room temperature and heated device frequencies at different power settings. In both curves, there is a clear transition where laser power does not cause an additional Stokes shift on the samples (flat portion of plots). For both cases, a sample laser power of roughly 50

μW (Figure 13) was found to not induce Stokes shifting to lower wavenumbers. Sourced laser power and neutral density filters were set to achieve this sample power level for device measurements. This threshold is highly device dependant and should be determined for each particular device.

4.1.2 Spatial and Spectral Resolution

The theoretical minimum diameter of a focused laser is far-field diffraction limited, and thus governed by the properties of the objective and beam (equation (2.1)). The diffraction limit is attainable with highly optimized optics, however, the actually limit degrades with laser mode or wavefront quality. Maintaining a non-diverging, collimated beam with a near-perfect Gaussian profile that properly fills the objective back aperture is necessary to reach this limit.

Spectra are collected from the entire area seen by the focused laser spot, deeming it the lower limit of the spatial resolution. Considering the NA of the 50X objective (0.75), the theoretical minimum spot diameter with a 488 nm laser line is approximately 325 nm, while the 50X LWD objective (NA: 0.55) is limited to a spatial resolution of 444 nm with its 8.2 mm working distance. The 100X LWD objective, used at Sandia National Laboratories (NA: 0.75) is capable of the same theoretical laser spot size as the 50X, and also has a working distance of 4.2 mm. This greater distance is an obvious advantage over the short working distance (0.37 mm) of the 50X when considering device packaging schemes, heated stages, etc.

The manufacturer of this system estimates its spot diameter at 700-800 nm, roughly twice the diffraction limit. In order to quantify the spot size, the laser spot was focused on a fixed knife edge, which was translated through the beam using the Pryor

translation stage (Figure 15). A step size of 0.1 μm was realized by using the stage for positioning. To account for hysteresis effects of stage control, measurements were recorded while moving the blade forward and backward through the beam. A ThorLabs power meter below the edge detected the transmitted power (15 mW sourced) not blocked by the blade. Power was then plotted against knife-edge position (Figure 16) for the 50X and 50X LWD objectives. It should be noted that the measurements in both directions are nearly identical. By using the Error function to the fit the data, the spot size was approximated as the distance of translation between 5 and 95% of the total transmitted power. Calculations yielded a focused laser spot size of 415 nm for the 50X and 525 nm for the 50X LWD. These values are 28 and 18 percent greater, respectively, than that of the far field diffraction limit. It was predicted that stage translation could have an uncertainty as high as 15 nm, leaving room for substantial error. While it is possible these preliminary measurements were under predicted by as much as 150 nm, a better concept of the micro-Raman system spatial resolution was obtained. A micro-positioner with higher resolution and perfectly straight travel would be an improvement over the current experimental technique.

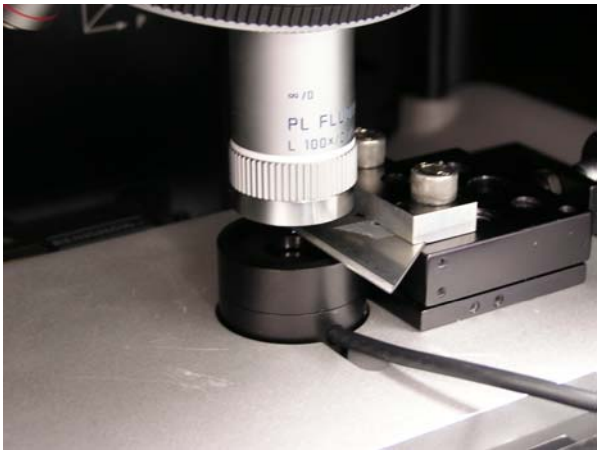

Figure 15. Experimental setup used for focused laser spot size measurement. A fixed knife-edge was translated through the focused laser spot, and the resulting transmitted power was recorded.

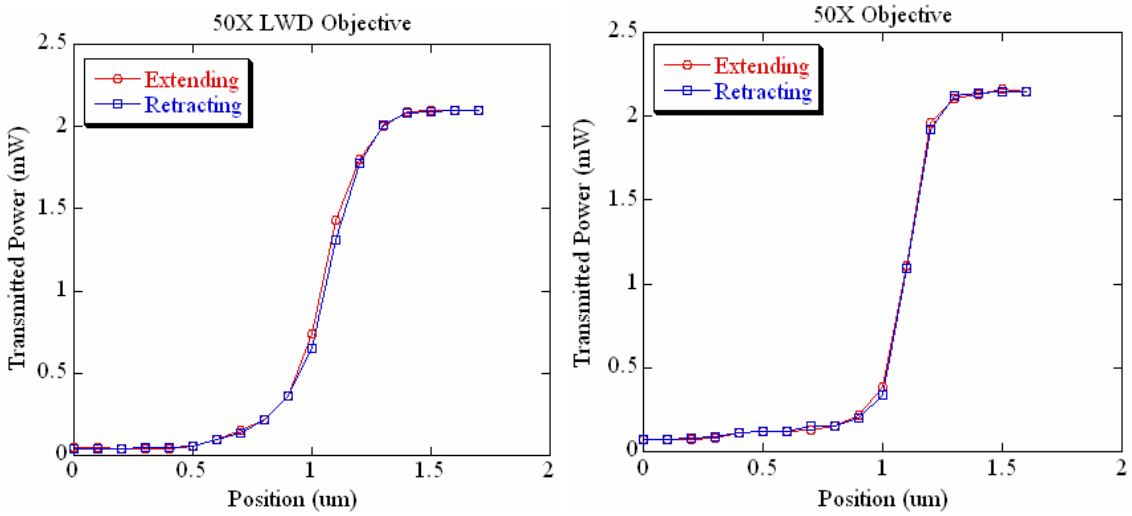

Figure 16. Results of laser spot size measurements.

In section 3.2, the effect of spectrometer slit width is discussed concerning spectral resolution. A slit width of 15 μm, in combination with the spectrometer focal length of 0.25 m and diffraction grating of 3000 lines/mm, resulted in a dispersion of 0.51 cm^{-1}/CCD pixel for the GT system and 0.9 cm^{-1}/pixel for the SNL system using a 65 μm

slit. Such dispersions are sufficient for determining small Raman frequency shifts and peak broadening in Silicon. The linewidth is instrument dependant; and is a direct image of the entrance slit after passing through the spectrometer optics. When the slit width is comparable or larger to the focused diameter of the collected Raman signal, the resulting image (linewidth) is affected. Figure 17 demonstrates the slit width dependence of doped polysilicon at room temperature on the SNL system. There is no affect until a slit of roughly 175 μm is reached, where the linewidth drastically reduces. By extrapolating the curve to a zero slit, the minimum detectable true linewidth of the first Raman transition is found as roughly 3.75 cm^{-1}, without any instrument bias. Do to the loss of signal magnitude, slit widths of 65 μm were used for some data of this study, specifically when larger ensembles of spectra were needed.

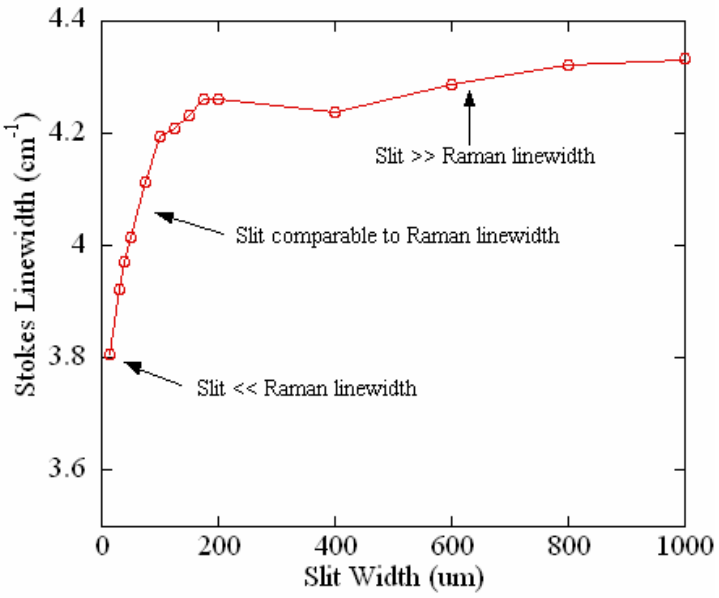

Figure 17. Instrument dependence of Stokes linewidth by varying spectrometer entrance slit width. The slit width drastically affects the linewidth of silicon when dialed to below 175 μm.

4.1.3 Photon Detection Efficiency

The light collecting efficiency of a microscope objective is a function of both its working distance and solid collection angle. This factor, the *f*/#, is the inverse of the numerical aperture. The solid collection angle is the conical volume of space seen by the objective, from which light is collected. Photons scatter from a surface throughout a hemispherical volume (red line in Figure 18). Thus, a larger solid collection angle (left, Figure 18) increases the collection volume, and percentage of collected photons. Theoretically, the collection angle of any objective is less than 180º (a hemispherical space).

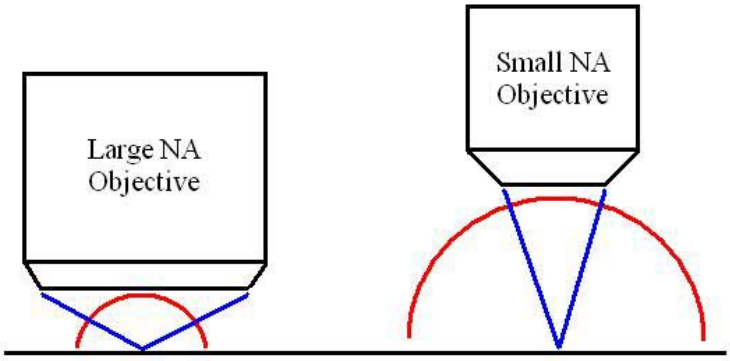

Figure 18. Visualization of light collection efficiency by varying solid collection angle of lens. A higher percentage of the scattered light field (red) is collected by a lens with a higher NA (smaller *f*/#).

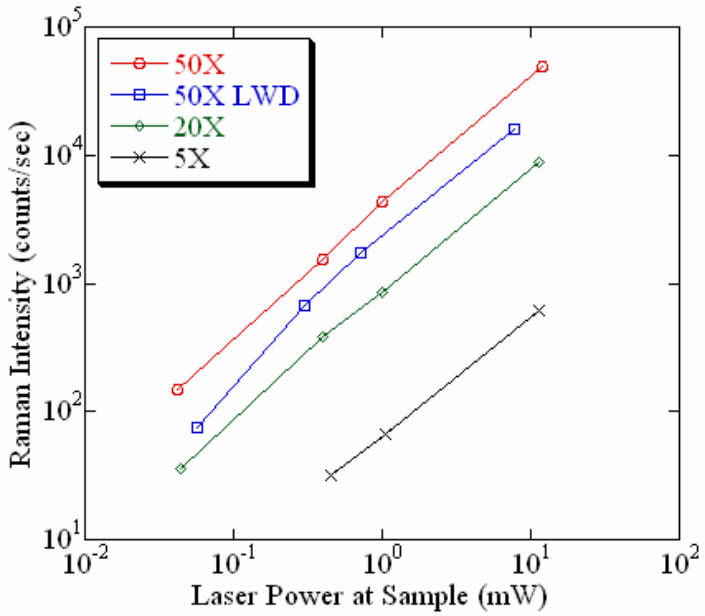

Figure 19. Raman intensity collected by each objective at various sample laser powers.

Figure 19 shows the Raman intensity of the Silicon Stokes peak at room temperature using various objectives, demonstrating that the amount of Raman counts is directly proportional to the amount of photons incident upon the sample. As seen, the choice of objective can vary the collected Raman signal intensity by orders of magnitude, decreasing the time required for steady state thermometry, and improving signal-to-noise ratios. A peak signal of 2000 counts was the minimum allowed for all measurements taken. At a given sample laser power, the 50X (and 100X) objective provides the highest light collection efficiency.

In short, the microscope objective, slit width, and laser power directly affect both spectra collection efficiency and resolution, and have been quantified in this section. Excellent spatial resolution and efficiency is provided by the 50X and 100X objectives, however working distance may become a factor with some devices. The 50X LWD

provides can accommodate more devices with its working distance, yet its lower NA results in longer integration times and a slightly larger focused laser spot.

4.1.4 Measurement Uncertainty and Drift Analysis

Throughout this study, peak location and linewidth of the first-order Stokes Raman resonance were used for temperature measurement. Therefore, uncertainty and reproducibility of the Raman method is limited by hardware and peak fitting software precision. In order to conduct a complete study of uncertainty, large ensembles of Stokes spectra (800-1000) were collected for a heavily P-doped polysilicon micro-beam at room temperature and 510ºC using the SNL Renishaw system. To quantify the peak signal-to-noise ratio, three data sets were taken at both sample temperatures with peak heights of 2500, 5000, and 10000 counts. A spectral curve-fitting code [84] using non-linear Voight functions provided batch processing for the peak frequencies and linewidths of the large data sets. These large numbers of data were needed to obtain a statistically significant sample size.

To process the data, a sixth order polynomial was fit to each set of data. This bias was subtracted from the experimental values to ensure the experimental mean was at zero. Histograms were generated for each set of position and linewidth data, to check that each data set resembled a normal distribution (Figure 20). Under these assumptions, a standard deviation was computed for each sample temperature/peak height combination. For a normal distribution, 95% of a sample set will be within two standard deviations of the mean.

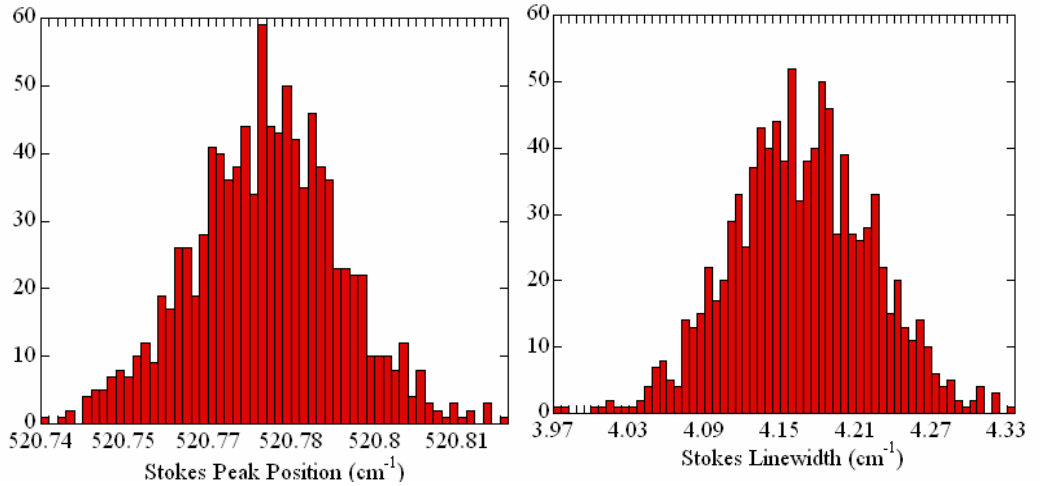

Figure 20. Typical histograms of statistical data of room temperature doped polysilicon beam: Left) Stokes peak position and Right) Stokes linewidth.

Following all data processing, the results of the peak position and linewidth estimators are found in Table 1. A clear trend favors the narrow peaks of a lower sample temperature and higher peak counts, as expected. This larger uncertainty can be attributed to wider peaks with lower SNR. Thus there is a trade-off between signal integration time and reduced uncertainty. The quantification of these data is used to calculate error in thermometry measurements in chapter 6.

Table 1. Stokes peak position and linewidth uncertainty estimators.

Stokes Peak Position			**Stokes Linewidth**		
Sample Temperature (ºC)	**Peak Counts**	**2σ (cm^{-1})**	**Sample Temperature (ºC)**	**Peak Counts**	**2σ (cm^{-1})**
23	2500	0.0641	23	2500	0.2704
	5000	0.0617		5000	0.2508
	10000	0.0266		10000	0.1112
510	2500	0.1317	510	2500	0.5831
	5000	0.1294		5000	0.5234
	10000	0.0923		10000	0.3547

Figure 21 displays the fitted peak Stokes peak location at the corresponding time of collection (room temperature sample, 10000 count spectra). A significant instrument drift (0.2 cm^{-1}) is seen to lower wavenumbers during this time span of four hours. There was no observed drift for the linewidth measurement in all data sets. No clear trend was visible when comparing the peak position over time for the large spectral sets. When making Stokes Raman measurements, it was determined that instrument drift is not predictable. Therefore, reference spectra should be retaken roughly every 8-10 minutes during Raman experimentation, to avoid error in measurement.

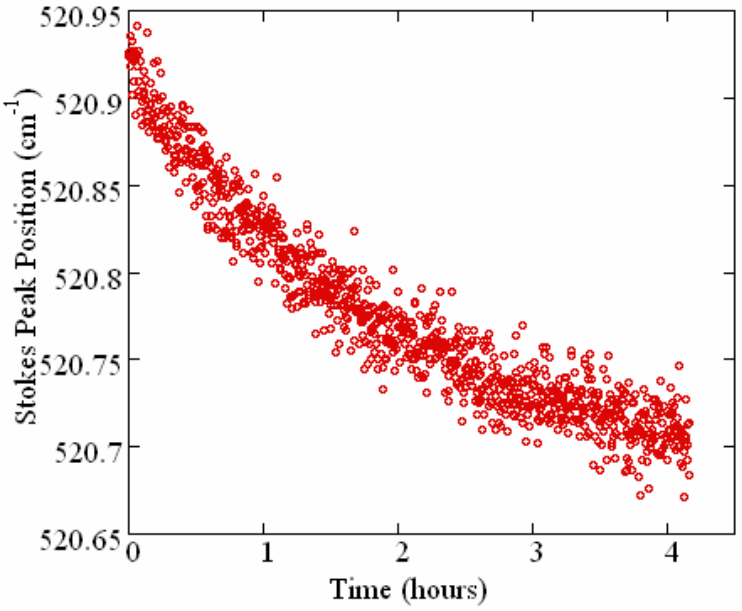

Figure 21. Instrument drifting of Stokes Peak position over time. Results of 1000 fitted peaks taken sequentially.

4.2 Fabrication Methods: Material Samples and Thermal MEMS

Samples tested in this study consisted of thin-films and simple thermal MEMS devices. Thin-films were deposited on Si-wafers and used calibrate the Raman thermometry technique as a function of polysilicon processing parameters. After the calibrations were performed, simple devices were fabricated on which temperature measurements were performed and compared with detailed thermal models. All material samples and devices examined in this work were fabricated in the Georgia Institute of Technology Microelectronics Research Center (MiRC) cleanroom. This section outlines the fabrication used for samples in this thesis, both for material property evaluation and device thermometry. While it is known microstructure and doping can alter the shape of Raman spectra, their affect on temperature response is not well documented. By altering processing parameters and doping, these issues were resolved.

4.2.1 Doped Polysilicon Samples

To begin, an STS PECVD (plasma enhanced chemical vapor deposition) system was used to deposit SiO_2 as a structurally sacrificial layer on <100> orientated 100 mm single crystal Silicon wafers. This recipe was used on 10 total wafers; where the oxide thickness for all samples was measured at 3.9 μm by white light interferometry. Following the SiO_2 deposition, polycrystalline silicon was grown on the SiO_2 film in a Tystar LPCVD (low pressure chemical vapor deposition) horizontal tube furnace. The following process conditions were used: SiH_4 flow: 1.7e-6 m^3/s, pressure: 26.664 Pa, temperature: 600ºC, yielding a polysilicon growth rate of roughly 10 nm min^{-1}. Polysilicon was grown on all substrates during the same process, insuring all films would have similar microstructural characteristics. Film thickness was revealed by vertically mounting a small wafer piece and applying a fine polish. SEM images were then taken of the cross-sectional area to verify the measurements of both the SiO_2 and polysilicon layers. A thickness of 4.1 μm was found for SiO_2, and 2.2 μm for the polysilicon.

In this study, it was desired to investigate the effect of various microstructures and doping concentrations of both Boron and Phosphorous in polysilicon on Raman thermometry. Table 2 indicates the variation of dopant species and amount for the set of wafers. The actual doping processing step was done by CORE SYSTEMS (Sunnyvale, CA), an independent vendor, specializing in ion implantation. With this technique, the depth of peak dopant concentration and surface concentration can be controlled with more accuracy than using an effusion cell doping process available in the MiRC facilities.

Table 2. Desired and predicted distribution of doped polysilicon samples.

Sample Number	Species and desired concentration (atoms cm^{-3})	Required Dose (atoms cm^{-2})	SSUPREM3 Predicted Concentration (atoms cm^{-3})
1	B, 1E16	4E12	2E16
2	B, 1E18	4E14	2E18
3	B, 1E20	4E16	2E20
4	P, 1E16	4E12	2E16
5	P, 1E18	4E14	2E18
6-10	P, 1E20	4E16	2E20

SSUPREM3, a diffusion software package, was used prior to the ion implantation to predict dopant concentration profiles. The software accepts input parameters such as implant species and dose, implantation angle and energy, and activation anneal temperature and time and calculates the volumetric doping concentration throughout the film thickness. Based on 200 keV of implantation energy, the software was used to find the required implant dose, SiO_2 cap thickness, anneal time, and temperature to obtain the desired uniform concentrations found in Table 2. SSUPREM3 yielded uniform distributions (Figure 22) using the following parameters to implant and activate the dopant species: 60 minute anneal at 1100ºC with a 100 nm thick thermally grown cap oxide.

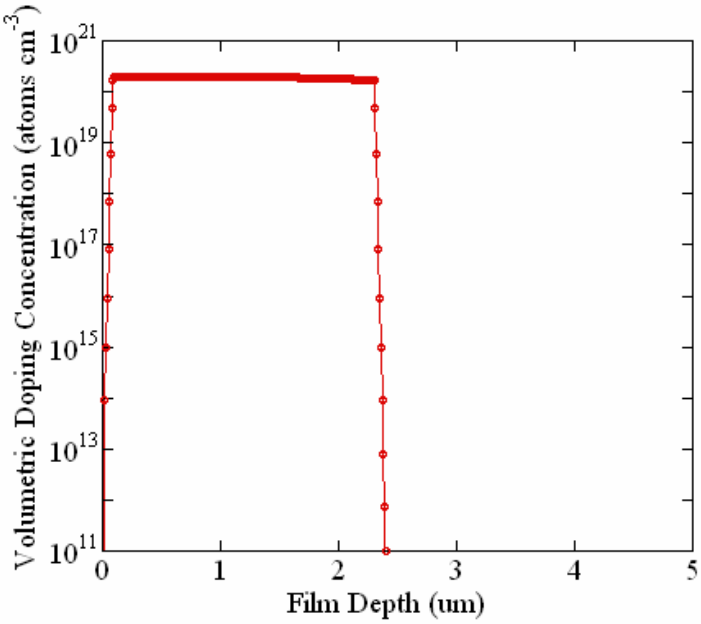

Figure 22. Example output of SSUPREM3, indicating uniform doping concentration throughout the polysilicon layer thickness (0.1-2.3 μm).

A cap SiO_2 was grown on the polysilicon films after receiving the wafers from the implantation vendor in a Tystar LPCVD furnace (850ºC for 2 hours). Due to the bombardment of dopant atoms during implantation, the polysilicon microstructure was damaged. Out-gasing of the implanted dopants was prevented by the SiO_2 cap film during the post-implantation, which annealed these defects. Following the annealing, the SiO_2 cap film was removed in a wet etch solution of 1:5 Hydrofluoric acid (HF) to water. Samples 1-6 were complete following the HF etch, while 7-10 were used to make thermal MEMS.

4.2.2 Undoped Polysilicon Samples

A similar approach was followed to prepare the undoped polysilicon samples. Similar silicon-on-insulator (SOI) film structure was used for this set of samples as well. 1-2 μm undoped polysilicon layers were grown at temperatures between 575 and 620ºC

on 1-2 μm thick SiO_2 films, as it is well known that this temperature regime provides drastically different polysilicon grain structures [85]. Again, annealing at 1100ºC for one hour insured stable microstructures on all samples. Samples from these wafers were used to investigate the effect of different microstructures on the stress and temperature calibrations. A single crystal silicon sample was analyzed as a reference. Table 3 presents the various undoped materials examined in this thesis.

Table 3. Variation of Undoped Polysilicon Samples.

Sample Number	Material
11	Undoped Polysilicon, 575ºC
12	Undoped Polysilicon, 588ºC
13	Undoped Polysilicon, 610ºC
14	Undoped Polysilicon, 620ºC
15	Bulk Single-Crystal Silicon

4.2.3 Device Fabrication

To conclude the fabrication portion of this work, polysilicon thermal MEMS with simply geometry were fabricated from the doped polysilicon-on-oxide wafers created in section 4.2.1. The devices of interest for this study are polysilicon micro-beams, which are capable of a broad range of temperatures due to resistive heating. Fabricated beam dimensions were any combination of length (100, 200, 300, 400, 500 μm) and width (5, 10, 20 μm). The contact pad dimensions in all cases were 1 mm by 1 mm, which provided sufficient area for creating electrical connections. Serpentine heaters were also

fabricated with the same process steps (see Figure 3). The heated atomic force cantilevers, which were measured as a part of this study, were fabricated with similar IC techniques, and the details can be found elsewhere [20]. The heavily doped polysilicon wafers (samples 7-10) were utilized for the processing of these devices (Figure 23). Although the following process schematics are not to scale, they provide a step-by-step visualization of fabrication techniques used to make the structures.

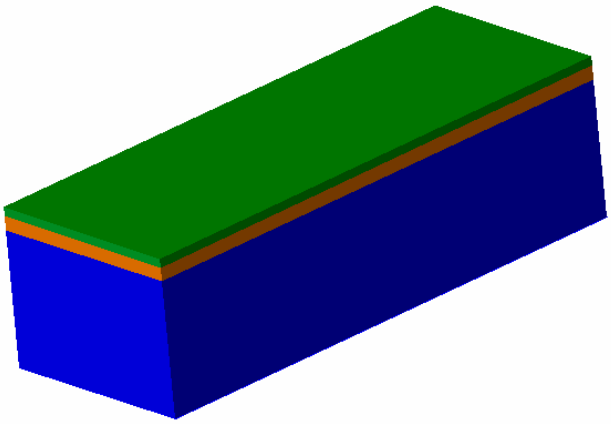

Figure 23. 3-dimensional schematic of polysilicon-on-insulator wafer (Blue: bulk Silicon Substrate, Orange: Silicon Dioxide, Green: Doped Polysilicon).

A two-mask process was used to create the devices. In the first photolithography step, Futurex NR-9 negative resist was used to pattern the beam/anchor pad assembly in the doped poly-Si layer. After development using Futurex RD-6, the photoresist mask was hard-baked for 15 minutes at 110ºC, insuring it could withstand plasma etching. A standard Bosch process, using a PlasmaTherm inductively coupled plasma (ICP) tool, was used to deep reactive ion etch the polysilicon. After removing the photoresist mask

with acetone and an oxygen plasma, only the doped polysilicon features remained on the oxide layer (Figure 24).

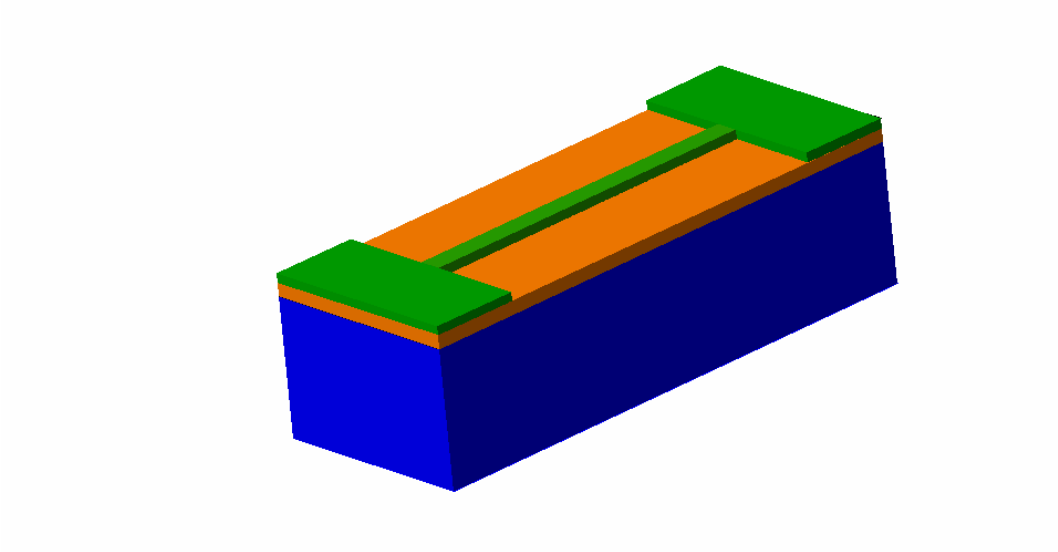

Figure 24. Beam and anchor pads following poly-Si etch.

The next process step involved aluminum metallization, which provided electrical connections to the polysilicon contact pads. A second mask was used following the polysilicon etch to define the pad geometry. AZ 4620, a thicker, positive resist was spun on the wafer and prepared appropriately. The mask was aligned with the present poly-Si features, and exposed with the required dose of 365 nm UV light. After development, 250-300 nm of aluminum was deposited using a plasma-sputtering tool. The wafer was then placed in acetone in an ultrasonic bath. The ensuing lift-off process left the aluminum pads remaining on the polysilicon anchor pads (shown as yellow in Figure 25).

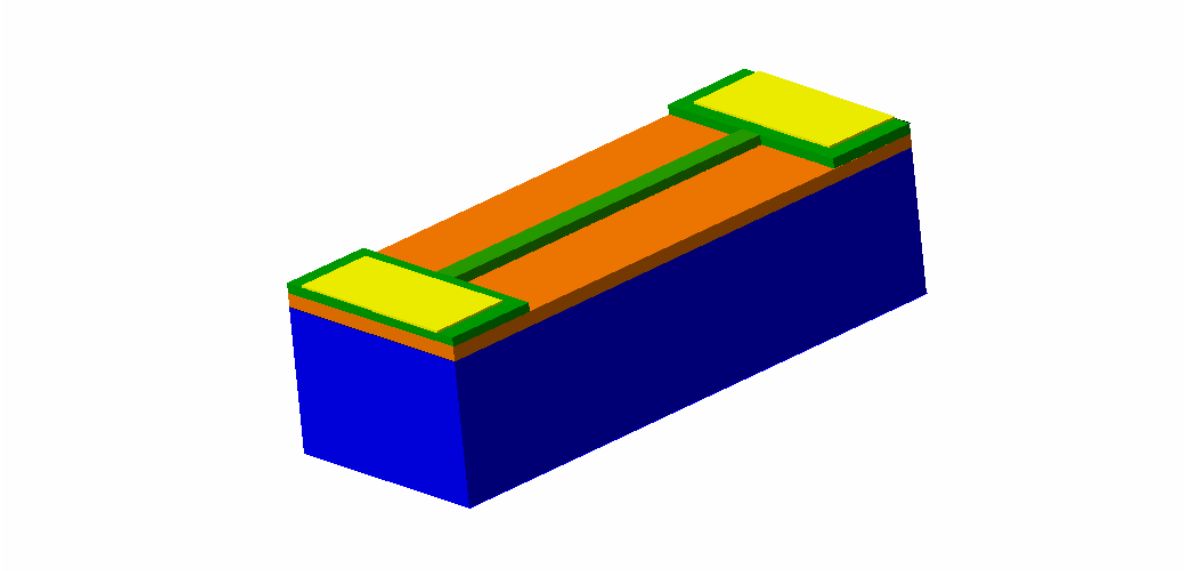

Figure 25. Beam and anchor pads following metallization lift-off process.

At this point in the processing, the wafer was diced, allowing all devices to be accessed separately. In order to compare the beam on oxide results with those of a suspended beam, a small set of beams underwent additional processing. The metal contact pads were masked using precisely placed acid-resistant tape. Samples were then placed in a 1:5 diluted HF solution, and given sufficient time for the acid to etch underneath and completely release the beam (Figure 26). Following the release, the samples were rinsed with DI water and immediately submerged in isopropyl alcohol, and then placed in a supercritical dryer. This final processing step completely removed any water that may have pulled the beams in contact with the substrate due to surface tension forces.

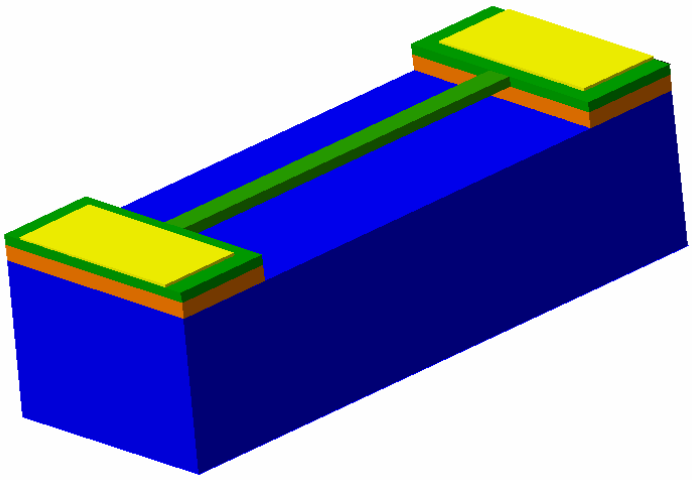

Figure 26. Beam and anchor pads following HF release.

Figure 27 is an optical microscope image of a completed beam on oxide, and Figure 28 presents an SEM micrograph, showing the air gap between the beam and substrate of a suspended structure. The analyses in the experimental sections utilizes Raman spectroscopy for both temperature and stress analysis of these structures.

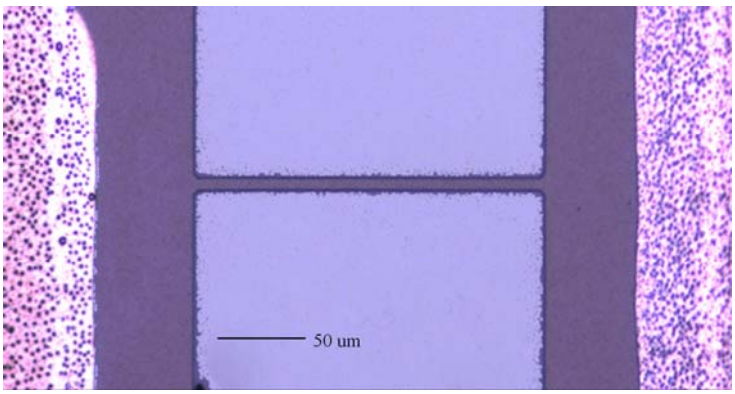

Figure 27. Completed 200 μm by 10 μm polysilicon micro-heater on oxide.

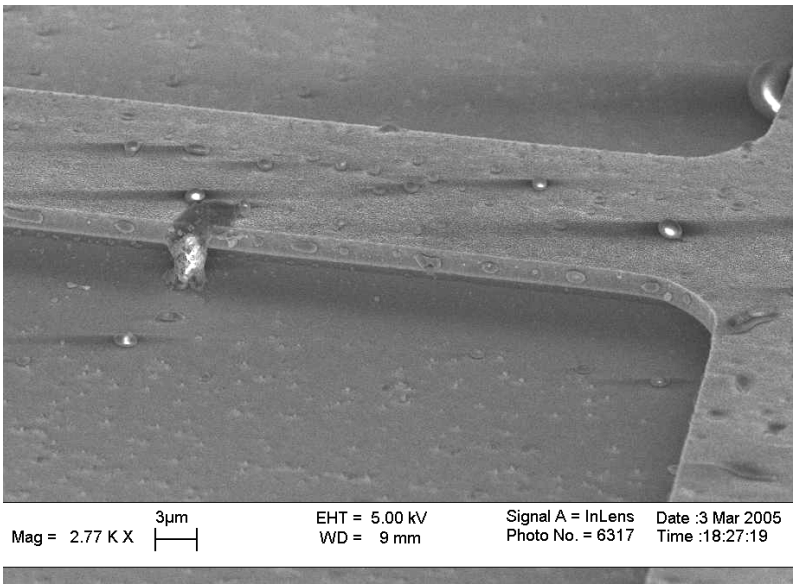

Figure 28. SEM image of a released 200 µm by 10 µm polysilicon micro-heated beam.

CHAPTER V

THERMAL METROLOGY OF SILICON MEMS DEVICES

In this chapter, the response of Si-based thermal MEMS was analyzed using Raman spectroscopy in addition to their electrical behavior. Heated AFM cantilevers and micro-beam heaters were chosen due to their wide range of applications in the development of a number of sensors, actuators, and scanning probe microscopy techniques. A range of thermal and mechanical boundary conditions are considered by studying both the beams and cantilever. The AFM cantilevers were fully released, with no underlying substrate and were expected to experience low thermal stresses during operation. The micro-beams were clamped-clamped structures between two large anchor pads, and either attached or released from an underlying oxide film. Both configurations constrained the expansion of the micro-beams; resulting in varying levels of thermal stress.

The validity of Raman thermometry was explored in-depth by the complementary use of Stokes peak position, Stokes/anti-Stokes ratio, and Stokes linewidth. Effects of thermally induced stress were taken into account and analyzed simultaneously. The two Renishaw Raman microscopes mentioned in chapter 4 were used to measure all devices in this portion of the study. Samples were probed with a 488 nm laser line, which was set to a sample power of roughly 50 μW based on the findings of laser heating in section 4.1.1. The 0.75 NA 50X and 100X objectives were utilized whenever applicable/possible

based on the system and sample type. In the final section of this chapter, finite element analysis (FEA) methods to model device behavior are introduced.

5.1 Temperature and Stress Calibrations for Thermal Metrology

As mentioned in the previous chapter, linear coefficients of both temperature and stress for the Stokes Raman shift have been reported with large variation for a number of processing and doping parameters. In addition, intensity ratio and linewidth calibrations are highly system dependant and should be done on the particular system. The following study addresses the effects of stress and temperature on the Raman signature in polysilicon processed under various conditions.

The initial calibrations in this section were done using the DilorXY Raman microscope at Oak Ridge National Laboratories (ORNL). This triple stage spectrometer has 180º backscattering geometry with a focal length of 800 mm and a grating of 1800 lines/mm, which yields a spectral dispersion of 0.346 cm^{-1}/CCD pixel when using the 514 nm laser line. The peak finding error in these measurements was found by measuring the Argon emission line multiple times and calculating a standard deviation of ±0.006 cm^{-1}. Laser power was measured at the excitation of the sample at 10 μW; this power level was determined to not cause localized sample annealing or heating effects (see section 4.1.1). All Raman spectra were fitted with Voight distributions using Labspec software.

5.1.1 Stress Calibration of Raman Signature

This section presents a more straight forward, concrete methodology to understanding the effects of stress on the Raman shift than seen previously in the literature. By inducing a known stress distribution on a sample, Raman spectra may be taken over the range of stresses. This eliminates the need for multiple samples with a

fixed stress state, where microstructural variation could cause error. Testing was performed using a 5000 N four-point bending fixture (Kammrath & Weiss, Dortmund, Germany). 40mm by 3mm beams (530 μm thick) were diced from all material samples (section 4.2), and used individually in the bending stage. The mechanics of a four-point bend and a large beam width to thickness ratio (6:1) helped to reduce out-of-plane bending. The load cell controller was closely monitored, assuring the crosshead displacement and applied load remained constant.

Each sample was loaded with a force of appropriate magnitude which resulted in a linear bending uniaxial stress distribution across the width of the beam from -300 MPa to +300 MPa. The loadings required to achieve this stress range were determined using classical beam theory. The largest moment, M, under 4-point bending occurs in the beam section between the two center contact points. Here, the moment is constant, and thus the beam experiences pure bending. Each center contact is one-eighth of the total beam length, L, from the end contact, thus M is given by equation (5.1).

$$M = \frac{FL}{8} \tag{5.1}$$

Where F is the force applied by the load cell in Newtons, and L is the beam length. The area moment of inertia is given by the simple relationship for a rectangular cross-section in equation (5.2), where t is the beam thickness, and w is its width.

$$I = \frac{tw^3}{12} \tag{5.2}$$

The largest normal stress of a beam in bending occurs at the largest distance, c, on the cross-section away from the neutral axis. In the case of simple rectangle geometry, this value is given as half of the beam width (equation (5.3)).

$$c = \frac{w}{2} \tag{5.3}$$

Normal stress at any point a distance y from the neutral axis of a beam in bending is given in equation (5.4).

$$\sigma = \frac{My}{I} \tag{5.4}$$

Therefore, by combining equations (5.1)-(5.3) and terms in equation (5.4), the maximum normal bending stress was determined in the beam at $y=c$.

$$\sigma = \frac{3FL}{4tw^2} \tag{5.5}$$

Equation (5.4) was then used to calculate stress across the beam width, which is linear between the maximum tensile and compressive values from equation (5.5).

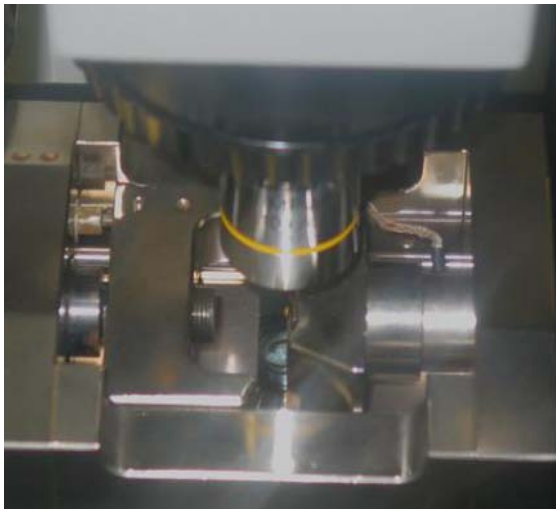

Figure 29. 5000 N four-point bending fixture with sample under the DilorXY800 Raman microscope.

As seen Figure 29, the bending fixture was placed on the sample translation stage under the Raman microscope objective, so that the excitation laser may be focused on the polysilicon film of the sample. Scans were taken sequentially at points 30 μm apart, across the width of the beam, yielding high resolution across the bending stress gradient. By traversing the beam in this manner, the entire range of uniaxial normal bending stresses was measured in a timely manner. First, scans were taken across the width of the unloaded beam to account for the effects of any residual stresses from processing. Immediately after, a second scan was taken at each of the same points of the loaded sample. Residual stress effects were removed by subtracting the unloaded Raman signature from the response measured under stress. This technique is valid based on the principal of superposition of linear elastic stresses.

5.1.2 Temperature Calibration of Raman Signature

A Linkam TS1500 environment controlled hot stage was used to maintain sample temperature for calibration of the Raman response (Figure 30). Small pieces (< 1mm^2) were cut from each sample for this work, to insure uniform heating over the entire sample. During the calibration, Raman spectra were recorded at each temperature from 23ºC (room temperature) to 1000ºC in increments of 100ºC. Three scans were taken and analyzed at every temperature step. The temperature calibrations of the Stokes peak were repeated for all material samples using the Renishaw Raman system at Georgia Tech with similar methods to those done at ORNL. The Doped polysilicon used for device fabrication was calibrated every 50ºC, to provide a finer data set for curve-fitting.

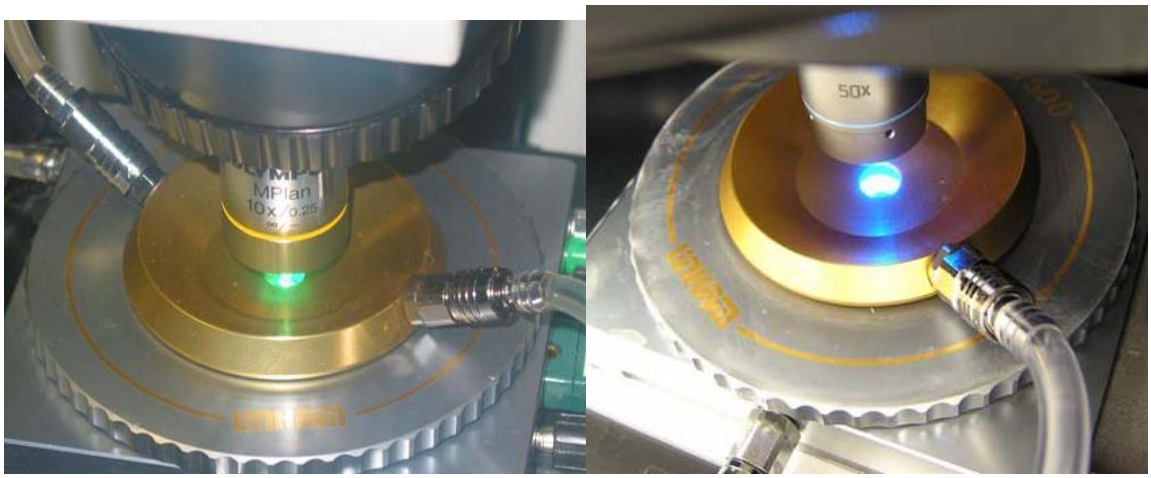

Figure 30. Linkam TS1500 temperature stage with sample under the Raman microscope objective: JY DilorXY800 (left) and Renishaw Invia Raman microscope (right).

A temperature calibration of the Stokes/anti-Stokes intensity ratio was performed on both Renishaw systems. Because this experiment is time consuming, it was done only on the heavily P-doped material that was used for device fabrication. During these calibrations, ten spectra were taken for both the blue and red-shifted Raman resonances, at the same increments used in the Stokes frequency calibration. Although long integration times limit the amount of collected anti-Stokes data, an estimate of the peak height ratio measurement uncertainty error was obtained across the temperature range. Background subtraction was used remove noise from all spectra, insuring accurate intensity measurements. Inverse temperature, in Kelvin, was then plotted against the intensity ratio to obtain the desired exponential fit (equation (3.6)). Curve-fitting was used to find the confidence levels of the ratio data.

Stokes linewidth was monitored across the same temperature range at Sandia National Laboratories. Again, a similar procedure was followed for data collection and curve fitting, averaging 20 spectra at each temperature. This reduced the uncertainty the scans by a factor of 0.22. A slit width of 65 μm yielded a spectral resolution of 0.9 cm^{-}

^{1}/pixel while keeping signal collection times reasonable. The same slit width was used for all thermometry measurements made using this technique. Data were fit using a parabolic function, as expected from the literature [76].

5.1.3 Microstructural Analysis

Knowledge of the microstructure of each sample was necessary to understand the differences in the temperature and stress coefficients found in the calibrations. An AFM was used to capture the 2-D surface topography of each sample. Small pieces of each sample were wet-etched in a buffered oxide etchant for 20-30s to clearly define the surface grain boundaries of the polysilicon films. After obtaining the material scans, an average grain size was determined for each sample.

5.2 Heated AFM Cantilever

The temperature distribution of a microfabricated atomic force microscope cantilever (similar to Figure 4) with an integrated heater element was measured, varying the power dissipation. These heated atomic force microscope cantilevers were introduced in chapter 1, and described in detail elsewhere [20]. A large electric resistance, due to selective silicon doping, causes high temperatures locally around the AFM probe tip with low power dissipation (< 10mW). The legs of the cantilever are Phosphorus doped to 1.93E20 atoms cm^{-3}, while the heater section, which connects the two legs, supports the probe tip and has variable doping.

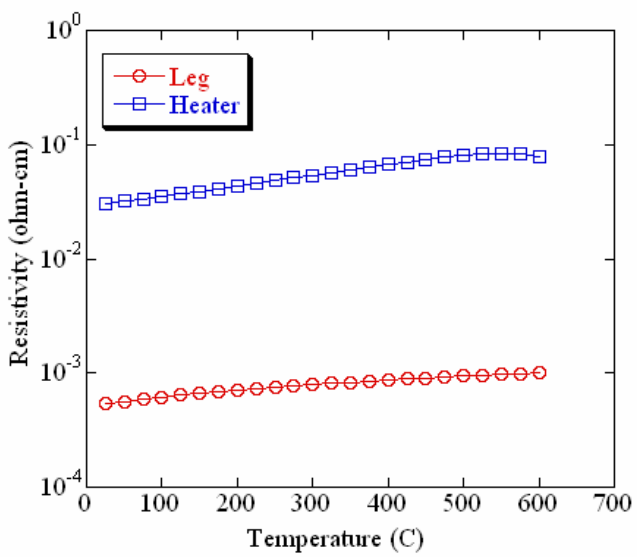

Figure 31. Temperature dependant electrical resistivity of the heated AFM cantilever. The heater region (blue) is selectively doped for a higher resistivity.

Though it does vary slightly, the average resistivity in the heater region is roughly two orders of magnitude smaller than that of the cantilever legs over a large temperature range (Figure 31). Figure 32 illustrates the variation of volumetric dopant concentration through the 600 nm thickness of the heater section.

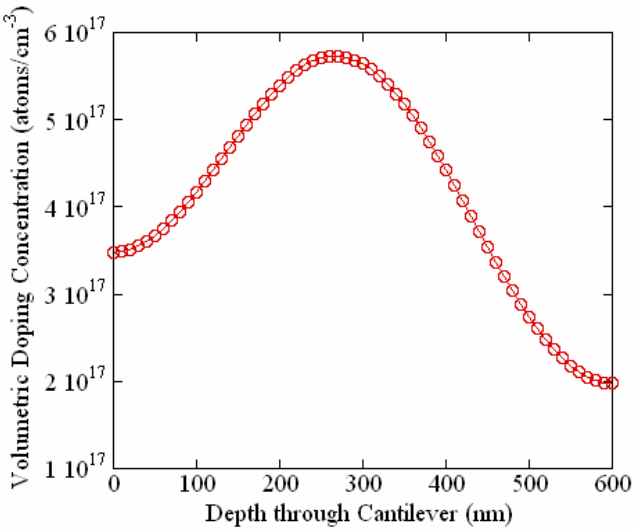

Figure 32. Variable doping throughout the thickness of the heater section.

Raman thermometry was performed at four points of interest along the heater region of the structure: the heater center (point 1), heater corner, heater/leg transition, and leg (point 4, Figure 33). These four points effectively characterize the temperature distribution from the heater region to the leg transition, which is directly related to device performance and overall functionality. An additional four points were measured every 22 μm along the 90 μm leg region of the device, to obtain a distribution of the entire structure. The same minimal laser power that was used for the material calibrations was used to avoid induced laser heating. Point 1 was also measured using the intensity ratio method over a smaller range of power dissipation. This was the only point monitored with the ratio calibration due to its functional importance. All other points were measured with only the Stokes resonance, as minimal thermal stresses were expected. Scan integration times were set to keep both Stokes and anti-Stokes peaks above 2000 counts.

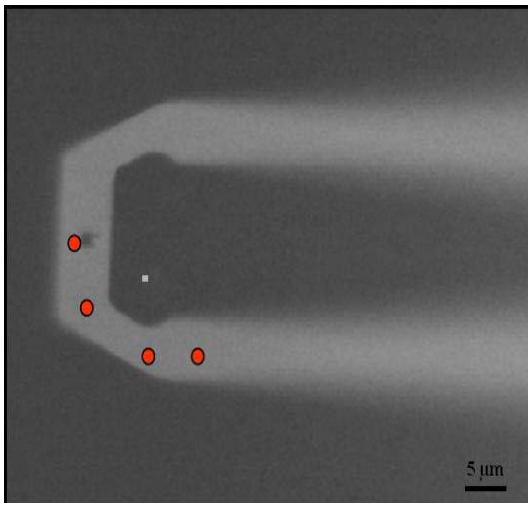

Figure 33. Location of Raman thermometry probed points on the heater region. Point 1 is at the center of the structure neat the probe tip, and points 2-4 follow in order away from the center.

The device was placed in series with a resistance of approximately 9.8 kΩ, which is comparable to the room temperature device resistance (~1.3 kΩ), and improves the sensitivity of the resistance measurements. A Keithley 2400 DC power supply sourced voltages in 1 V steps from 0 to 0.5 V below its maximum operating voltage. The last four data points taken were in 0.5 V steps, as the device resistance changes drastically in that range. The cantilever resistance as a function of sourced voltage was found using an Agilent 34401A multimeter to measure voltage drop across the sense resistor. Device power dissipation and resistance was then calculated using elementary circuit theory based on the sourced and sense resistor potentials.

After data collection, the spectra were fitted using the Renishaw Wire2.0 software. Because the Stokes calibration coefficient, K_{stokes}, is strongly linear with temperature, a simple relationship was used to find corresponding temperatures.

$$T = T_{ambient} + \frac{\omega_{ambient} - \omega_{measured}}{K_{Stokes}} \tag{5.6}$$

Where T is device temperature, $\omega_{ambient}$ is the reference Stokes frequency at $T_{ambient}$, and $\omega_{measured}$ is the Stokes frequency of the powered device.

5.3 Polysilicon Heated Micro-Beams

This section presents a Raman study of the polysilicon heated micro-beams fabricated in section 4.2. Again, the devices chosen in this study were meant to provide a different combination of thermal and mechanical boundary conditions as compared with the heated AFM cantilever.

5.3.1 Comparison of a Released and on-oxide Heated Beams

The following study of doped polysilicon devices was a comparison of a released beam and one residing on an underlying oxide film (unreleased). The performance of these thermal MEMS is directly affected by this structural aspect, since the mode of heat dissipation from the device is primarily through conduction and radiation. The thermal conductivity of the SiO_2 insulating film is greater than that of air by over an order of magnitude. Thus, by removing the oxide under the beam, the thermal dissipation path it provides is no longer present, increasing the rate of change of temperature with respect to power dissipation. In both cases, the beams are clamped on each end, while the oxide presence establishes an additional constraint along the length of the unreleased beam.

Both beams under examination had dimensions of 200 by 10 μm for an accurate comparison. Sample 1A consisted of an unreleased straight beam, and Sample 1B was released (Figure 27 and Figure 28). Wafer curvature measurements by contact profilometry revealed bowing that placed the polysilicon layer in residual tensile stress. This stress was expected to vary with the Joule heating. Sample 2A is a serpentine heater also fabricated on oxide layer (Figure 3), with equivalent dimensions to that of a 645 x 10 μm straight beam. Both wire bonding to an electronic package and a custom built probe station were used to provide a sourced voltage to the microdevices. Figure 34 shows the focused laser spot of the Renishaw system on a 10 μm wide polysilicon beam on oxide.

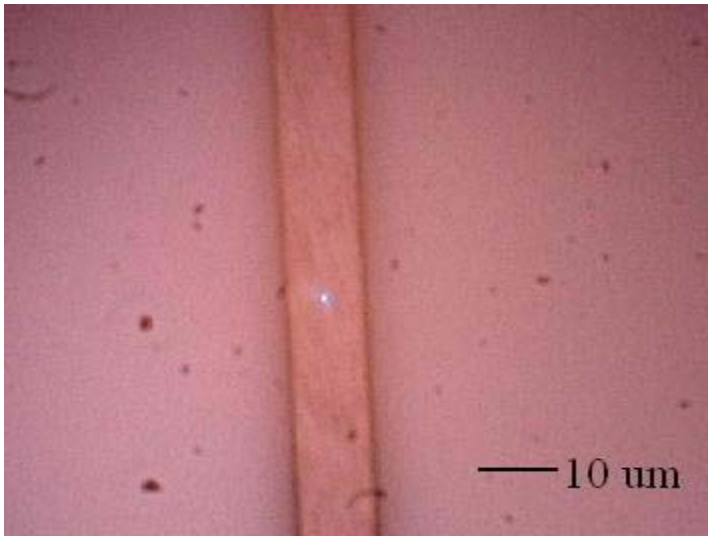

Figure 34. Focused laser spot on 10 μm wide polysilicon beam using the 100X objective.

Raman scans were performed in a similar fashion to those present in section 5.1. A sense resistor of 100 Ω, comparable to the room temperature resistance of the beams (~130 Ω), was used for the same reasons as with the AFM cantilever. Stokes and anti-Stokes spectra were taken at the center, varying the device power dissipation. By comparing the intensity ratio calibration with that of the Stokes, an estimate of thermally induced stresses may be realized. Equation (5.6) was used to find temperature using the Stokes coefficient, while the exponential calibration of the intensity ratio was used to back-out temperature at the same power dissipation.

5.3.2 Beams on Oxide: Distribution and Linewidth Measurements

Preliminary stress calibrations of polysilicon thin-films reveal that the Stokes linewidth is insensitive to stress. For this reason, the final investigation of the micro-beams involved comparing thermometry measurements based on Stokes frequency and linewidth. The use of linewidth to investigate thermal stresses is a highly desired

capability, as its advantages over the intensity ratio include integration time, calibration range, and sensitivity.

Based on the results in section 4.1.4, the linewidth measurement uncertainty is roughly a factor 4-5 times greater than that of the Stokes peak position. As an initial measurement, the repeatability of the linewidth was quantified to reveal the sources of this uncertainty. Twenty spectra were collected three times in a day, at four locations (located in a 5 by 5 μm square) on sample 3A (similar to Sample 1A). This revealed information as to the effects of localized microstructural changes and instrument dependence.

It was also deduced that the excessive heating of the micro-beams may induce slight grain growth in the microstructure, and alter the linewidth during a set of measurements. This aspect was analyzed by taking 30 room temperature spectra at the beam center. Sample 4A was used, again similar to Sample 1A, which had not been powered previous to the experiment. A voltage was applied to the device that was predicted to cause a center point temperature of 100ºC. After holding this temperature for 6-8 minutes, the power was switch off, and 30 spectra were again recorded at room temperature. This thermal switching was done every 100ºC up to 900ºC, recording room temperature spectra each time.

To conclude this portion of the experimentation, the beam center of Sample 3A was measured as a function of device power dissipation. Measurements were taken at every 1V step, from 0-15 V. Twenty spectra were taken at each power setting to reduce the data uncertainty, and temperature was calculated based on the respective calibration types. To measure the temperature distribution of the beam, a power was set to yield a

predicted 400ºC at the beam center. Spectral sets were collected twice at each point, for both the reference and powered cases. Points 5 μm apart were measured near the anchor pad, were a large gradient was expected, while this distance was increased to 10 μm closer towards the center. The analysis of the data gave insight to temperature and thermal stress behavior, both across the beam length for a given power and at the beam center as function of power.

5.4 Finite Element Analysis

In order to compare experimental data with theoretical calculations, the FEA packages of ANSYS Classic v7.1 and ANSYS MultiPhysics v9.0 were used to model the heated silicon MEMS devices. Models were built with Thermal-electric coupled-physics elements, which accept an applied voltage across the geometry, and solve for the resultant temperature distribution. Similar studies have used finite difference techniques over simplified geometries with shape factors [8, 20], however, this modeling technique solves the complete 3-D heat conduction equation using the appropriate thermal-electric properties and boundary conditions. Temperature dependant thermal conductivity was supplied as a look-up table in ANSYS based upon data for single crystal silicon, doped silicon and polysilicon, and air found in the literature [8, 20, 86, 87]. The data for silicon from these references were modeled using a Boltzmann phonon transport model with a relaxation time approximation in order to predict the thermal behavior of the doped silicon materials at higher temperatures. Grain size is expected to dominate the variation of thermal conductivity, over that which is due to doping, across the measured polysilicon materials. The thermal conductivity of the PECVD silicon dioxide was measured using a modified 3-ω experiment [88]. Electrical resistivity was modeled as a

function of Phosphorus doping level and temperature [20], and the resulting values were also used as an input for the FEA model. The temperature dependent resistivity code made use of the relationship in equation (5.7).

$$\rho(T) = \frac{1}{q\mu(T)N(T)} \tag{5.7}$$

Here, q is the electron charge, μ is the electron mobility, N is the number of intrinsic carriers and T is the temperature. The calculations of the model were based on the temperature dependent mobility for phosphorus doped polysilicon [89]. In order to account for the variable doping of the AFM cantilever in the depth direction, the heater section was divided into 12 volumes of 50 nm each. Resistivity was then found for the average doping levels for each 50 nm increment. A uniform, dense mapped mesh was used both throughout the micro-beams, and in the air/oxide surrounding the beams. However, the complicated geometry of the cantilever structure made meshing more difficult. A dense mesh was used throughout the heater and leg transitions in order to capture large thermal gradients, while only light mesh was needed for the legs (Figure 35).

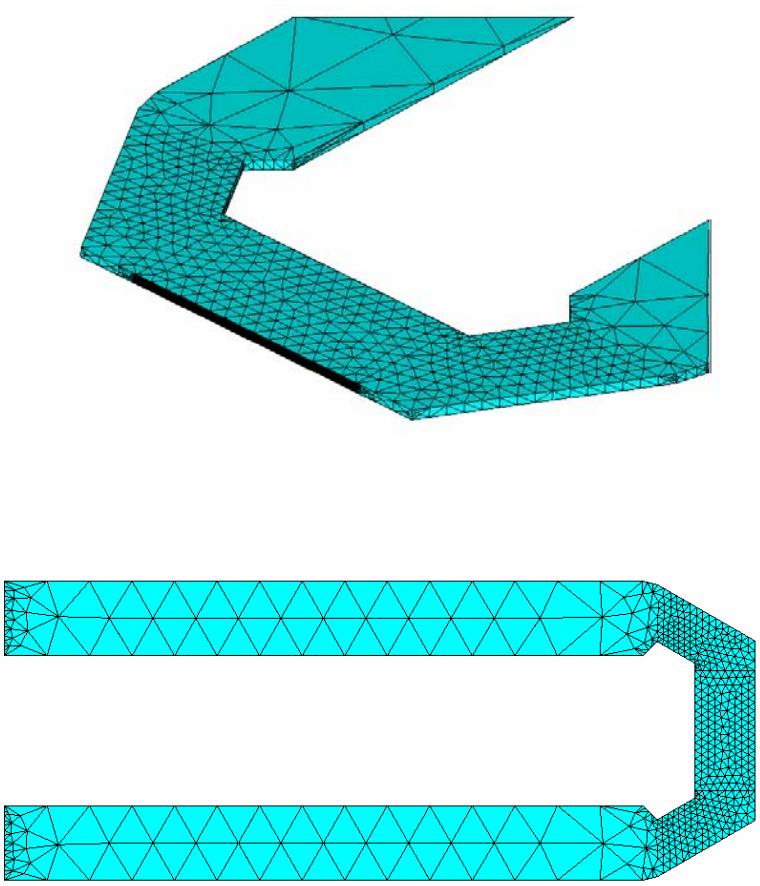

Figure 35. Meshing schemes used for cantilever geometry. Top) Zoomed-in view of heater section. Bottom) Full geometry.

Both the thermal conductivity and electrical resistivity were modeled from 22-800ºC for the analysis. Heat loss due to radiation heat transfer with the ambient was applied as a boundary condition to all surfaces of the powered devices, with an assumed emissivity of 0.8. This value was based on micro-IR experimentation and assumed constant over the experimental temperature range. While heat loss by natural convection is negligible for micro-devices of these dimensions due to small Rayleigh numbers [90], conduction heat transport into the surrounding air was found to be the dominating mode of heat loss. The mesh surrounding the devices has the thermal conductivity properties of

air to account for this. For the suspended structure, radiative losses to the substrate also have a significant effect, and were included on both surfaces.

For the cantilever, a constant temperature boundary condition over the cross-sectional areas at the ends of both legs was assumed. This is a valid assumption, as the resistive heat source of the cantilever is isolated from the clamped ends. This is not the case in the micro-beams, where heat loss to the anchor pads is expected to be significant. For, this reason, the pads were included in the modeled geometry. A voltage drop was applied to the end surfaces of each structure.

The model was then run for the same input voltages that were measured in the Raman experimentation. In order to correctly model these devices, details of the doping level are needed; yet only estimates from the SSuppreme model are known. Thus, model estimates were used as an initial guess, which was adjusted until the power dissipation from the FEA models matched that of the experiments. Differences may be attributed to the uncertainty of the actual implant dosage as performed by the outside vendor. When modeling temperature distributions, half-symmetry was used to reduce calculation times.

CHAPTER VI

EXPERIMENTAL AND THEORETICAL RESULTS

Experimentation and modeling results are presented in this chapter. The following sections provide evidence of the capabilities of Raman spectroscopy as a microscale thermometry tool for Si-Based MEMS. The first section presents and discusses the results of the temperature and stress material calibrations. Second, thermometry results of the heated AFM cantilever are presented. Detailed data from the polysilicon micro-beam experimentation are shown in the following section. The chapter is concluded with a comparison of experimental data and FEA analysis.

6.1 Temperature and Stress Calibration Results

The hydrostatic stress of a loaded structural member is the average of the stresses applied in each coordinate direction, given by equation (6.1).

$$\sigma_{Hydrostatic} = \frac{\sigma_{xx} + \sigma_{yy} + \sigma_{zz}}{3} \tag{6.1}$$

For the uniaxial pure bending case, as seen with the Raman stress calibrations in section 5.1.1, only normal bending stress in one direction is present, and the relationship reduces to equation (6.2).

$$3\sigma_{Hydrostatic} = \sigma_{xx} = \sigma_{Uniaxial} \tag{6.2}$$

The measured coefficient, B_{Stokes}, can be used to directly calculate stress, for a known uniaxial case, following equation (6.3) where $\Delta\omega=\omega_{Loaded}-\omega_{Unloaded}$.

$$\sigma_{Uniaxial} = \frac{\Delta\omega}{B_{Stokes}} \tag{6.3}$$

For most thermal MEMS devices, the plane-stress assumption can be made, which assumes a non-zero displacement (zero-stress) in the z-direction. By making this assumption, it may be possible to estimate bi-axial stress values using the Raman coefficient. However, an in-depth mechanical analysis is necessary to accurately use Raman for stress distribution determination. Therefore, following the practice found in the literature of presenting the value for hydrostatic stress, the measured coefficients were multiplied by a factor three. This relationship is shown in equation (6.4) by combining equations (6.2) and (6.3).

$$\sigma_{Hydrostatic} = \frac{\Delta\omega}{3B_{Stokes}} \tag{6.4}$$

Table 4. Measured Stokes Linear Coefficients of Temperature and Stress

Sample	Dopant (Species, atoms cm^{-3})	ORNL Stokes Stress Peak Shift (cm^{-1} MPa^{-1})	ORNL Stokes Temperature Peak Shift (cm^{-1} $^oC^{-1}$)	GA Tech Stokes Temperature Peak Shift (cm^{-1} $^oC^{-1}$)
1	B, 2E16	-0.002155	-0.0231	-0.0233
2	B, 2E18	-0.003731	-0.0233	-0.0232
3	B, 2E20	-0.001870	-0.0230	-0.0234
4	P, 2E16	-0.002934	-0.0231	-0.0232
5	P, 2E18	-0.002317	-0.0228	-0.0229
6	P, 2E20	-0.003805	-0.0222	-0.0227
11	Undoped	N/A	-0.0221	-0.0234
12	Undoped	-0.003618	-0.0224	-0.0229
13	Undoped	N/A	-0.0228	-0.0231
14	Undoped	-0.002878	-0.0226	-0.0231
15	Undoped	-0.002859	-0.0222	-0.0235

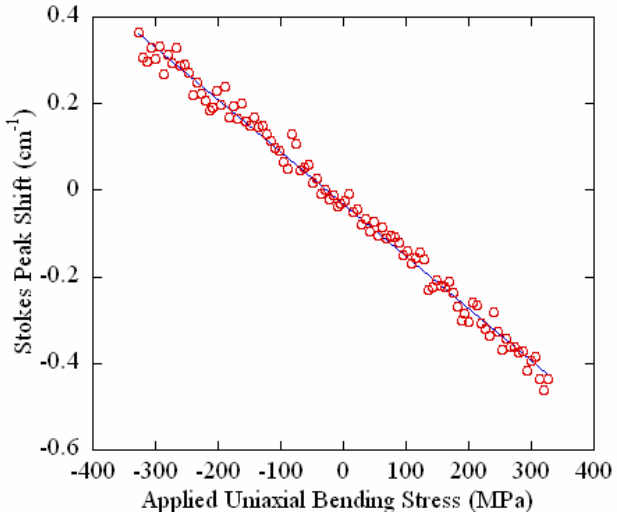

Figure 36. Typical plot of Stokes stress calibration. Undoped polysilicon grown at 588ºC is shown.

It is clear from the resulting data that the Raman shift coefficients due to hydrostatic stress show some variability across samples, ranging from -0.00187 to -0.003805 cm^{-1}/MPa (a representative calibration shown in Figure 36). While no clear trend in this parameter as a function of sample processing is observed (Table 4), the impact of these results should not be lost. These data are based on single measurements at each point, and thus measured peak shifts due to stress are on the order of the 2σ uncertainties reported in Table 1. Repeating the calibrations with multiple scans would reduce calibration uncertainty, thus any variation seen between samples would be better accepted. Additional variation may be a result of defect density in the materials which would require transmission electron microscopy analysis for confirmation. For all data, the results shows two things when analyzed closely: 1) The shift is quite small for the amount of stress that is applied and 2) it has a second order effect on the Raman shift due to the method in which stress distributions in the polysilicon effect the deformation in the silicon lattice. Thus, the effect of stress may be ignored in most cases unless very large

stresses are present in the device. Many thermal MEMS devices utilize suspended structural designs; changes in stress are much lower than changes in device temperature.

Upon further investigation of the stress calibration data, it was determined that the linewidth was unaffected by the applied loading. As seen in Figure 37, the linewidth data is scattered about its mean by roughly ±0.06 cm^{-1} across the entire stress range measured. This is well within the 2σ uncertainties of room temperature linewidth data from Table 1.

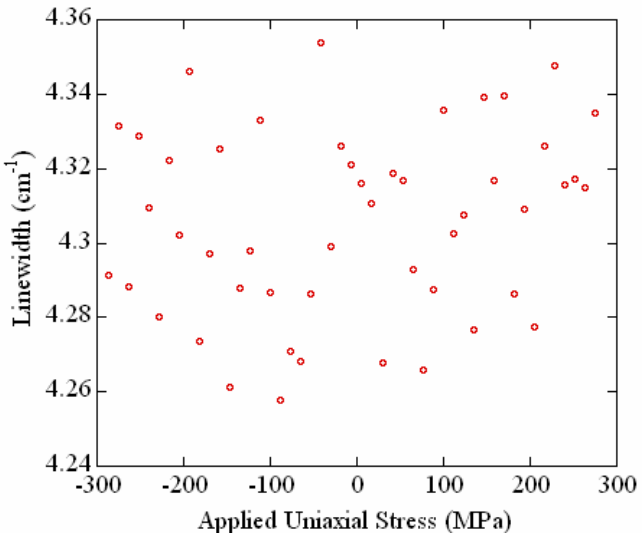

Figure 37. Effect of stress on the linewidth of doped polysilicon. The scatter of the linewidth with stress is far less than the measurement uncertainty.

For all samples, simple linear relationships with strong correlation coefficients ($R^2 \geq 0.99$) were observed. Thus, more rigorous curve fitting of the temperature data using equation (3.7) was not necessary. A review of the Stokes temperature coefficients indicates that the peak shift is much more sensitive to temperature effects than stress. This is due to the uniform expansion of the silicon crystals upon heating, which does not occur with stress as a result of elastic anisotropy. All temperature coefficients remain

linear between room temperature and 1000°C (Figure 38), which allows for very easy calibration of temperature over a broad range; a capability not available with other methodologies. In addition, the information given is a comparison of coefficients from different Raman systems and excitation wavelengths (514 and 488 nm). Though differences in the temperature Stokes coefficients fall within the peak-fitting uncertainty, a given material should be calibrated using the particular system and wavelength. Otherwise, direct use of these coefficients may result in some slight error.

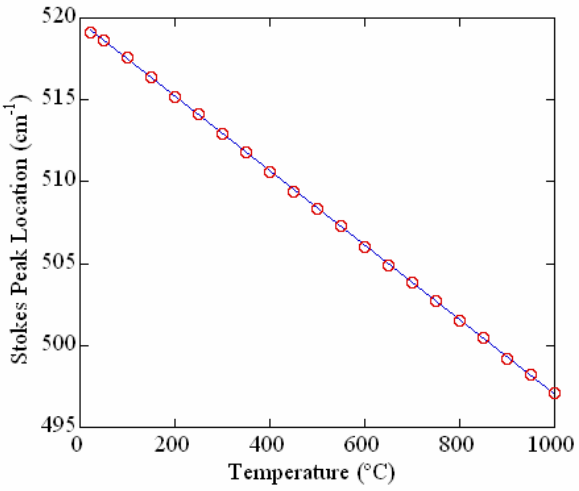

Figure 38. Representative Stokes Peak temperature calibration (P-doped polysilicon). A near-perfect linearity of this temperature calibration is found from room temperature to 1000ºC.

Overall, lower temperature coefficients are found for undoped materials as opposed to doped samples. Slight changes between the boron doped and phosphorous doped materials are seen as phosphorus tends to segregate to the grain boundaries during annealing, affecting the phonon scattering process differently than uniformly distributed boron. It is believed that the presence of a high density of defects or scattering from

dopants may affect the optical phonons near the zone center, giving rise to some process dependent Raman coefficients. Such effects have been seen in nanocrystalline silicon where coefficients vary greatly from single crystalline materials [55].

6.1.1 Polysilicon Linewidth and Intensity Ratio Calibrations

As mentioned in chapter 3, the Stokes/anti-Stokes intensity ratio is a function of only temperature; independent of applied stress. Results from the previous section indicate the Stokes linewidth is unaffected by stress as well. Figure 39 displays a good parabolic fit to the calibration data ($R^2 > 0.98$) in the form of equation (6.5), where Γ is the Stokes linewidth. Parameters A, B, and C were found as 4.605E-6, 0.008011, and 4.258, respectively, from the data fit and used for the calculation of device temperature, by solving the ensuing quadratic equation.

$$\Gamma(T) = AT^2 + BT + C \tag{6.5}$$

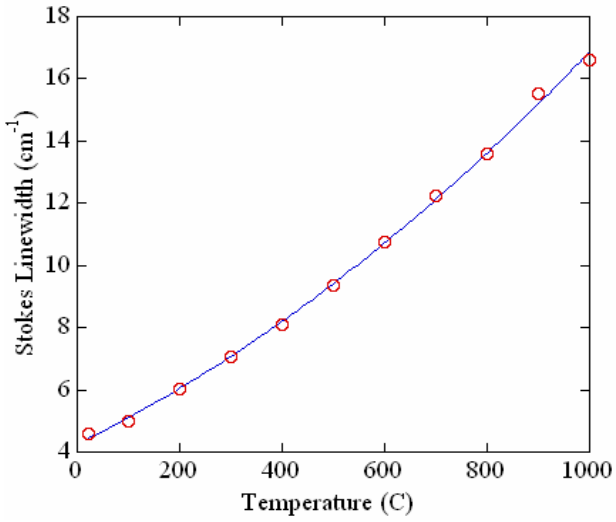

Figure 39. Temperature calibration of the Stokes linewidth with temperature. This method exhibits a strong parabolic fit, and was shown to be independent of stress.

Similarly, results of the doped polysilicon intensity ratio calibration are seen in Figure 40. A sufficient data fit to inverse temperature (K^{-1}) was realized when using the exponential form of equation (3.6). Peak heights from the fitted spectra were used for the ratio calculations; however a comparison of the integrated spectral areas would reduce uncertainty in these measurements. Parameters Q and P were calculated from the data fit of the doped polysilicon, as 1.793 and 700.29, respectively. Similar values (1.7754 and 732.53) were obtained for the calibration of single crystal silicon. Device temperature of laser probed points was then found based on the signal intensity ratio, *I(T)*, as described earlier.

$$I(T) = Q\exp(PT) \tag{6.6}$$

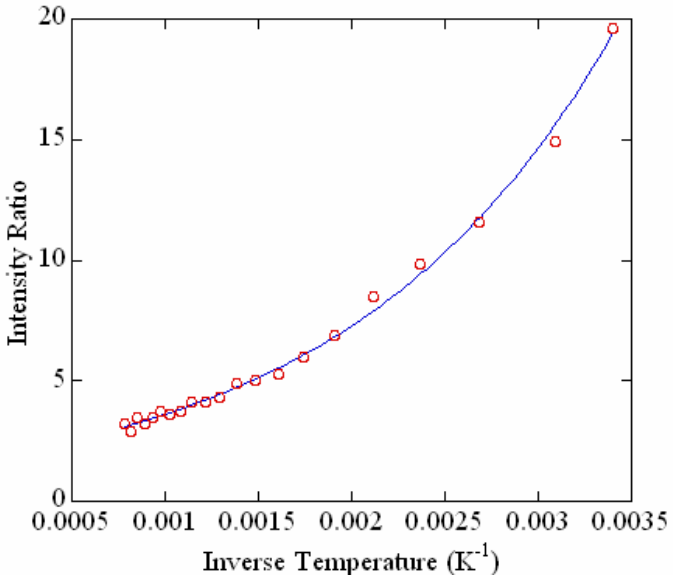

Figure 40. Temperature calibration of intensity ratio for doped polysilicon. Data was plotted against inverse temperature to obtain the exponential fit found in equation (3.6).

6.1.2 Microscopy Analysis Results

Estimates of the average surface grain size for all polysilicon samples are listed in Table 5. These data only depict measurements of surface grain size from AFM scanning (Figure 41). The measured grain sizes all have values above 100 nm, eliminating phonon confinement effects on the scattering measurements. Thus, variations in grain size should have no effect on Raman behavior, only defect density. Therefore, results indicating the Raman shift versus temperature for the undoped Silicon reference and polysilicon samples are similar is not surprising. It is also seen that the doped samples behave in a similar manner as the single crystalline doped materials.

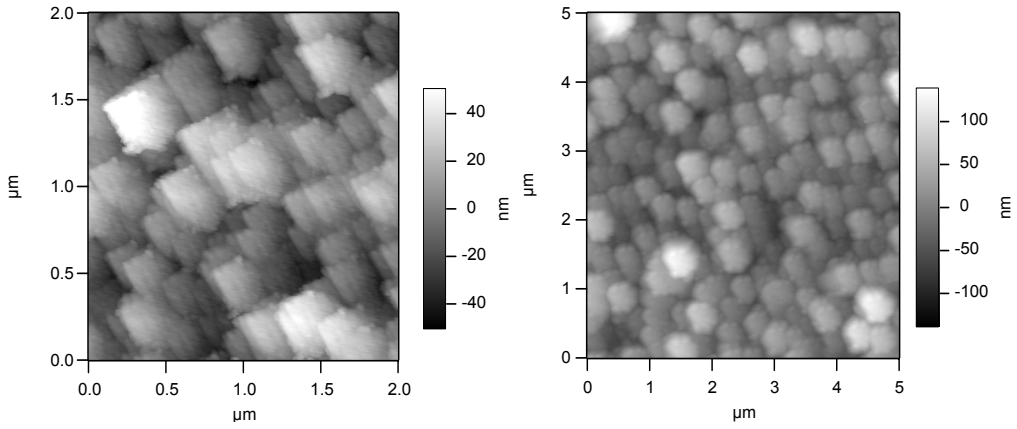

Figure 41. Sample AFM Scans of Polycrystalline Silicon.

Table 5. Average surface grain size of polysilicon samples using an AFM.

Sample ID	Average Grain Size (nm)	Sample ID	Average Grain Size (nm)
1	280-320	6	220-260
2	155-195	11	200-240
3	300-340	12	230-270
4	350-390	13	130-170
5	200-240	14	280-320

6.2 Thermometry of a Heated AFM Cantilever

Results of the experimentation in section 5.2 are discussed in the following section. The maximum operating voltage of the system circuit was determined as 15.5 V (across cantilever and sense resistor). As seen in Figure 42, the resistance increases with sourced voltage until it reaches 15.5 V. Here, the device experiences thermal runaway, which results in resistance drop with increasing temperature. The resistance values were recorded with the Raman laser incident upon the cantilever. This is important to account, because the laser produces photoelectrons in the silicon lattice, causing an increase in circuit current.

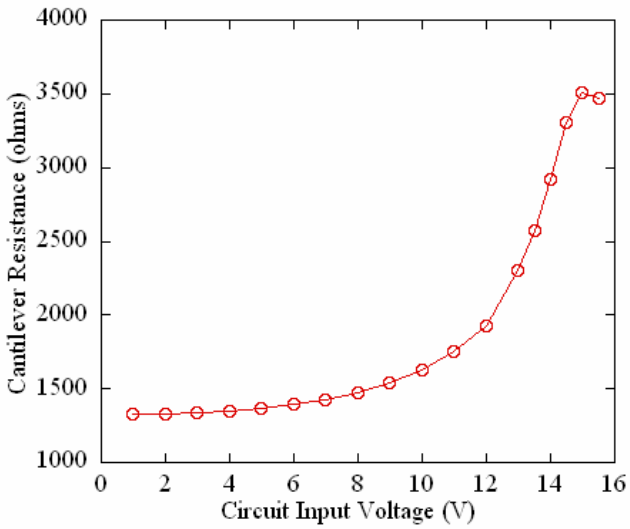

Figure 42. Electrical Response of the heated AFM cantilever

The sample was able to reach a maximum temperature near 650°C with an input power of 4.8 mW, as measured in the center of the heater region by the Stokes method. Based on the uncertainty data of Table 1 (excluding instrument drift), measurement error this technique across the entire range did not exceed ±5ºC. A comparison with the Stokes/anti-Stokes intensity ratio method indicates a near exact match of the heater center temperatures (Figure 43). The difference between the two techniques never exceeds 10% over the entire test regime with a maximum difference of 21°C at 3.45 mW. It is important to note that a deviation between the two techniques is first seen at temperatures near 450ºC. As mentioned earlier, this is the temperature regime where the ratio calibration increasingly loses sensitivity with greater temperature. From ratio calibration data, it was determined the uncertainty in temperature measurements below 500ºC is ±21.3ºC, which is on the order of the deviation seen. For this reason, it is possible the difference in the measured temperatures from the two techniques is due to a) thermally

induced stresses in the heated device or b) experimental error in the intensity ratio measurement.

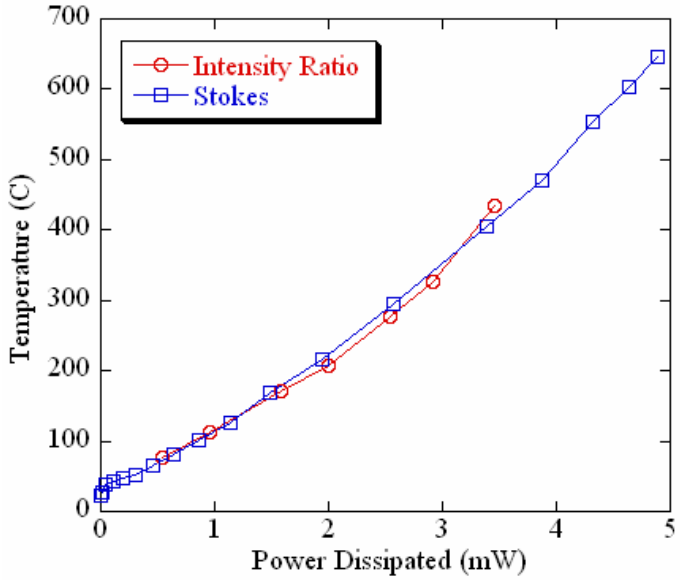

Figure 43. Temperature of the heater center as a function of power center using the Stokes position and intensity ratio calibrations.

Assuming the deviation is due to induced stresses, corresponding hydrostatic stress magnitudes may be calculated. Following this assumption, the temperature given by the intensity ratio calibration is converted to an equivalent Stokes peak position. The difference of the two Stokes temperatures is then converted into a Raman shift (in cm^{-1}) using the temperature calibration coefficient. Thus, if the method that only depends on temperature (intensity ratio method) has a lower equivalent Raman peak position than the Stokes method (higher temperature), then the sample is in a state of compressive stress; a tensile stress would be true for the opposite case (Stokes method higher temperature than intensity ratio). As can be seen in Figure 43, the intensity ratio temperature begins by reaching lower temperatures than predicted by the Stokes method with increasing power.

The temperature/power slope of the ratio method then increases, and yields a higher temperature than the Stokes peak at the highest power that was examined. Following the above explanation, these data indicate the cantilever first reaches a tensile stress of roughly +110 MPa, then transitions to a compressive state of stress of -170 MPa at higher temperatures. This change in stress state can be attributed to out of plane caused by thermal expansion. A constrained 'U' shape with variable heating has the capability to achieve this sort of stress state. This method should be used as a qualitative assessment, as the uncertainty in these measurements is not fully quantified.

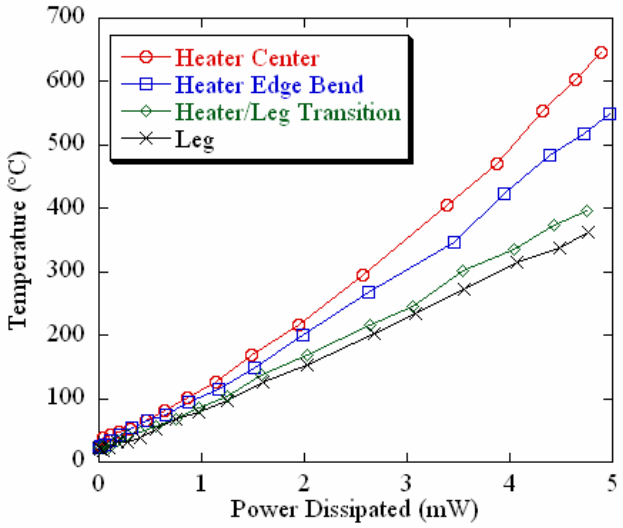

Figure 44. Temperature of probed points in the heater section of a Heated AFM cantilever.

The temperature at the four probed points, found using the Stokes linear temperature coefficient in equation (5.6), are seen in Figure 44 as a function of dissipated power. Intuitively, the center point reaches the highest temperature, while points further away reach lower temperatures as the distance away from the heater is increased. Based

on the measurement comparison done at the heater center, it was determined the intensity ratio method was not needed for accurate thermometry on the additional probed points.

The depth of penetration of the 488 nm laser line is approximately 700 nm, and thus the entire thickness of the cantilever is probed by the beam. This is important, because the values of stress found from the comparison in Figure 43 are averaged over the entire thickness of the device, not just its surface. This was also noticed during the experimentation as changes in input power caused out-of-plane motions as determined by the need to refocus the microscope moving the objective closer to the sample. At higher powers, it is possible that the magnitude of the compressive stress will increase. However, accurate determination of this can not be made due to the increased uncertainty at higher temperatures.

6.3 Thermometry of Polysilicon Heated Micro-Beams

A review of the data of polysilicon beam Samples 1A, 1B, and 2A is presented in this section. Device resistance increases more gradually than seen with the electric response of the heated cantilever (Figure 45).

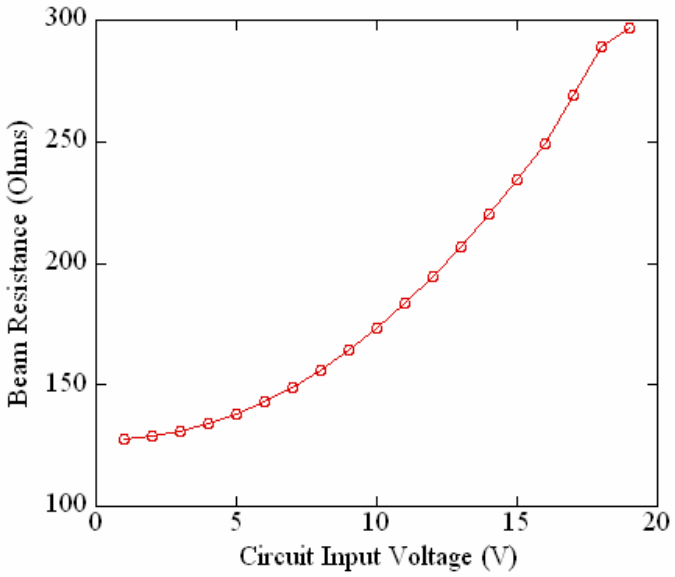

Figure 45. Electrical response of a polysilicon beam on oxide (sample 1A).

Following these procedures, the safe operating range for all three devices was determined. Figure 46 displays the temperature response of the straight polysilicon beam on oxide, Sample 1A, as a function of power dissipation. The sample reached a temperature on the order of 450°C with an input power of 275 mW, as measured by the Stokes method. A comparison with the Stokes/anti-Stokes intensity ratio method indicates that stress may be affecting the temperature measurements most notably at higher input powers where the measurements deviate. However, this deviation between the two techniques never exceeds 10% over the entire test regime with a maximum difference of 40°C at 275 mW.

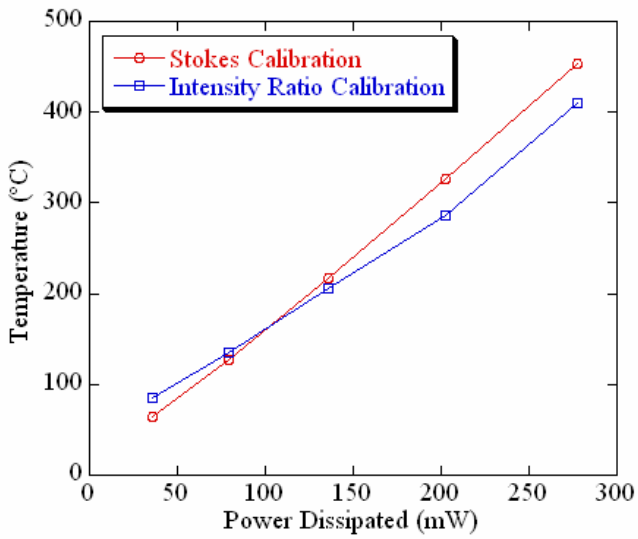

Figure 46. Comparison of Raman thermometry methods at the center of sample 1A.

Changes in stress in the sample are determined by the method presented in the previous section. The stresses predicted by this technique are then superimposed on the original stress state in the samples. The data show that while heating, the sample experiences a superimposed compressive stress due to the constraints of local expansion. However, as this force grows with increasing temperature, the measured tensile stress in the sample increases from 150 to near 650 MPa, following equation (6.4). Again, this type of stress quantification is based on preliminary results, and is in need of additional calibration data for verification.

The reasoning for this increasing tensile behavior is explained as follows. Due to the fabrication of the sample, the oxide layer places the silicon substrate in residual tension. This causes the wafer to bow and flex the thin-films on the upper surface of the wafer. This curvature places the top portion of the polysilicon layer in residual tension. Since the Raman system is operating at 488 nm, its depth of penetration is only 700 nm, well above the neutral axis of the entire system. Thus, tensile residual stresses are

recorded in the polysilicon. As the beam heats, addition flexure of the sample is induced, causing an increase in the tensile stresses due to bending. Again, it was necessary to refocus the objective as changes in input power caused out-of-plane motions. As the sample continues to heat it is expected that the rate at which the stress increases will change due to the heating and thermal expansion of the oxide layer underneath the polysilicon layer. Thus, the two measurement techniques are not always expected to diverge. The effects of the change in these constraints for multilayer thermal MEMS devices are difficult to model due to uncertainty in high temperature mechanical properties.

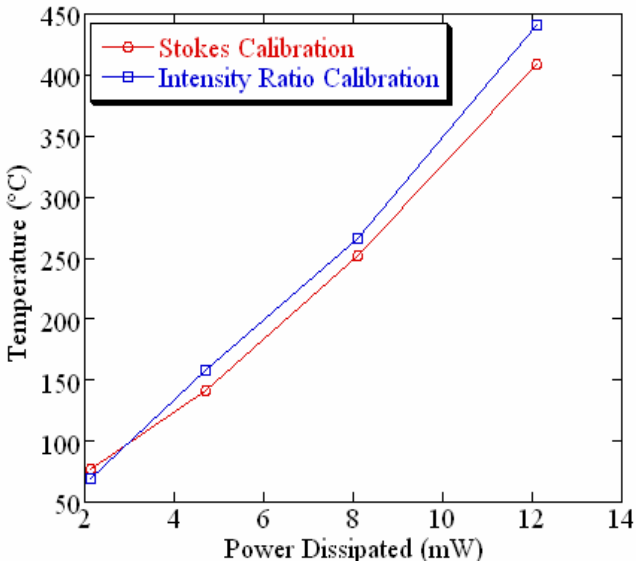

Figure 47. Comparison of Raman thermometry methods at the center of sample 1B.

Figure 47 displays the results of temperature measurements on the released beam center (Sample 1B). The data also show an ability to reach 450°C, but with an input power of 12 mW (20 times less than Sample 1A). The comparison of the Stokes method

to the Stokes/anti-Stokes ratio technique show much closer agreement, being a maximum of 7% difference at the highest temperatures. Again, the polysilicon structure is in residual tension, but for a different reason. It was noted that this residual stress was dependent on the etch release step which undercut the oxide anchors on the electrical contact pads. As the undercutting is performed, the polysilicon layer is released and allowed to contract (due to the higher coefficient of thermal expansion) and place the beam under residual tension (Figure 48).

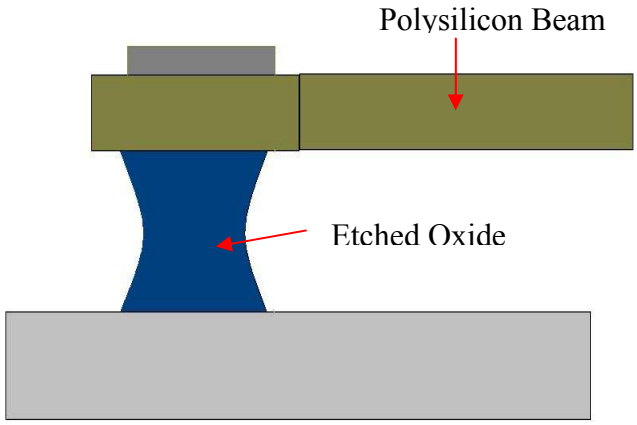

Figure 48. The HF release step undercutting Silicon Dioxide sacrificial layer, placing the polysilicon beam in residual tension.

As the structure is heated, only compressive stresses build due to the constraints and are superimposed on the residual tensile stress. This is noted by a steady drop in the tensile stress of the beam. The beam is nearly stress-free at the highest heating powers. Again, relatively good agreement between the two thermometry methods is demonstrated throughout the entire test regime. For both samples, the measurement deviation between methods at temperatures above 400ºC is larger than the uncertainty of ±21.3ºC.

Therefore, additional measurements are necessary in order to determine the source of the variability in the stress measurements and their repeatability.

Figure 49 presents results of Sample 2A using only the Stokes frequency method. These results were made based on the relatively good agreement between the techniques outlined at the beginning of this section. Due to its low power density, significantly more power is required to reach the same temperatures as Samples 1A and 1B.

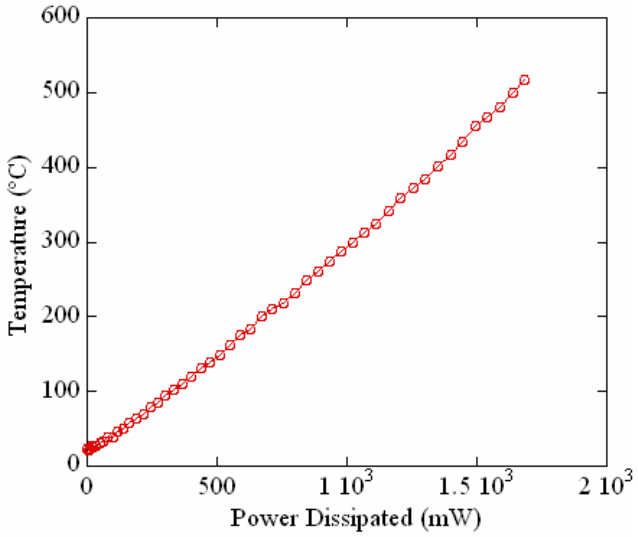

Figure 49. Temperature as a function of power dissipation, as measured at the center of Sample 2A using the Stokes position method.

The use of linewidth to investigate temperature and thermal stresses is a highly desired capability, as its advantages over the intensity ratio include integration time and near-constant sensitivity across a broad range of temperatures (23-1000ºC). Based on the results in the first section, the linewidth measurement uncertainty is roughly a factor of 4-5 times greater than that of the Stokes peak position. After an initial investigation, the repeatability of the linewidth was quantified to reveal location dependant sources of

uncertainty on Sample 3A. Differences in linewidth greater than the 2σ uncertainty, by at most 0.03 cm^{-1}, resulted when comparing measurements from four locations on the beam. This type of scatter adds an additional uncertainty to linewidth thermometry, and is most likely due to microstructural variations in the polysilicon.

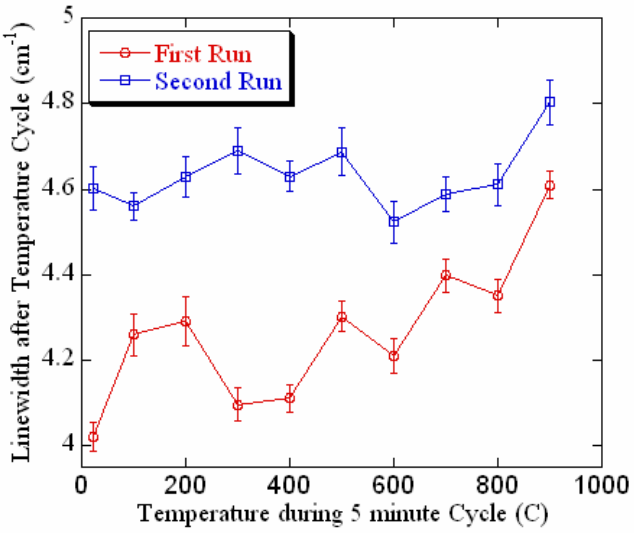

Figure 50. The effect of thermal cycling on linewidth measurements. A polysilicon beam (Sample 4A) was heating to each temperature, held for 5 minutes, and then cooled to room temperature where linewidth data were taken following each heating step.

An increasing trend in linewidth (Figure 50) was seen during the first thermal cycling set on Sample 4A, as described in section 5.3.2. During the second run, a leveling-off occurred, which indicated a slight annealing of the polysilicon device may have occurred after the first set of temperature steps. Larger grains and the segregation of dopant atoms to grain boundaries are a possible result of this. Although a temperature of 900°C is not expected to alter the microstructure of polysilicon drastically, it is possible

the changes in linewidth are directly related to the material response of high temperatures.

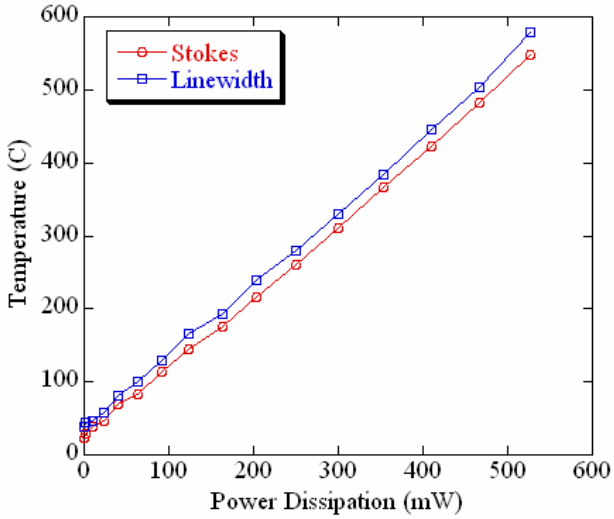

Figure 51. Temperature of fixed-fixed beam center as a function of power dissipated. When comparing the Stokes and linewidth techniques, a thermally induced compressive stress was realized.

Figure 51 compares the Stokes and linewidth thermometry calibrations on the center point of Sample 3A, which are within 8.5% of each other across the entire power dissipation range. The Stokes shift method under predicted temperature when compared to that of the linewidth; attributing this difference to thermal stress results in a prediction of an induced compressive stress state. The length of the beam is fixed to the surface, thus out of plane bending does not occur. Therefore, it is possible that the beam may have experienced pure axial expansion, resulting in a compressive stress. As discussed previously, the linewidth measurement introduces additional uncertainties; however, efforts were made to reduce these by taken multiple scans at each point. Figure 52 shows a measurement technique comparison of the temperature distribution of Sample 3A with

322.15 mW power dissipated. The data indicate the largest difference at the beam center, as seen with the center point measurement versus power. However, the gradient from the anchor pad (distance of 0 μm) to 40 μm shows excellent agreement between the two techniques. This suggests an increasingly compressive hydrostatic stress gradient as the beam center is approached, while a constant stress across the length is expected. Deviations are not expected to be due to measurement uncertainty, as the linewidth error in this case is ±7ºC. More structural analysis is warranted for the acceptance of these discussions. Without further knowledge of the stress distribution, such results cannot be verified.

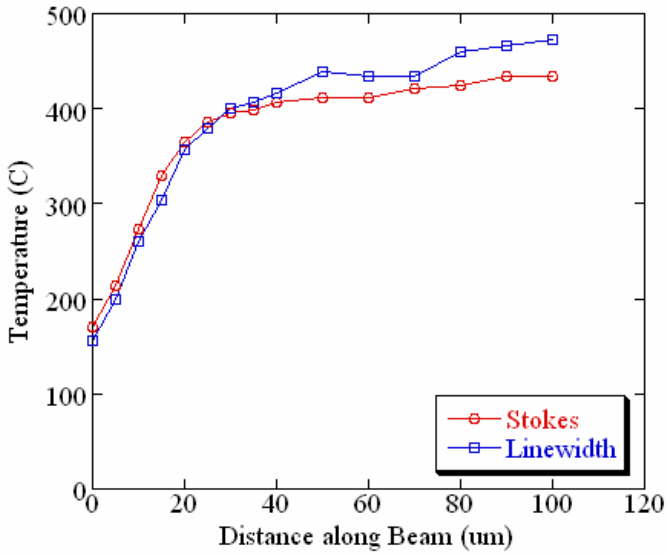

Figure 52. Temperature distribution of a fixed-fixed beam (Sample 3A) using half-symmetry. A comparison of the Stokes and linewidth calibration is seen, revealing an excellent match near the bond pad (distance = 0) and a significant difference (40ºC) at the beam center (distance = 100).

6.4 Finite Element Analysis Results

For the mutli-physics finite element analysis, it was found that both the electrical and thermal behavior must be modeled in order to provide accurate predictions of device behavior. To do this, the voltage placed across the samples was used as an input to the finite element model and the calculated power dissipation was compared to each experimental value. The comparison of the model and experimental data show good agreement over the entire range of input voltages for both the AFM cantilever and beam on oxide (Figure 53). This model takes into account the temperature dependent thermal conductivity of all materials involved and the electrical resistivity, as explained in the previous chapter.

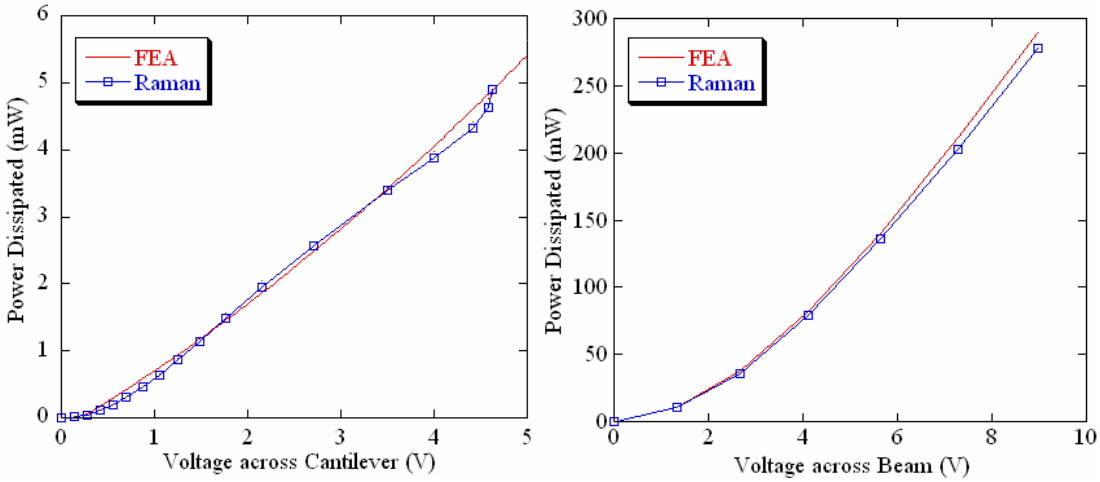

Figure 53. Comparison of experimental and FEA electric response of thermal MEMS devices. Left: Heated AFM cantilever, Right: Beam on oxide (Sample 1A). This comparison insured similar power dissipation for a given input voltage.

Once this result was verified, the thermal response of the heated cantilever as predicted by ANSYS was compared to the experimental measurements at the device center point. The calculated temperature values are within 9% of the Stokes shift

measured values across the entire input power range for the heated AFM cantilever (Figure 54). After verifying an agreement for the thermal response of the heater center, the distribution using half symmetry was compared for a power dissipation of 3.9 mW (Figure 55). Of the eight probed points across the 110 μm length, the largest deviation of the model from the Raman thermometry is less than 10%. Figure 56 is a graphic of the temperature distribution calculated by the FEA software. The hot spot of the heater section is clearly visible.

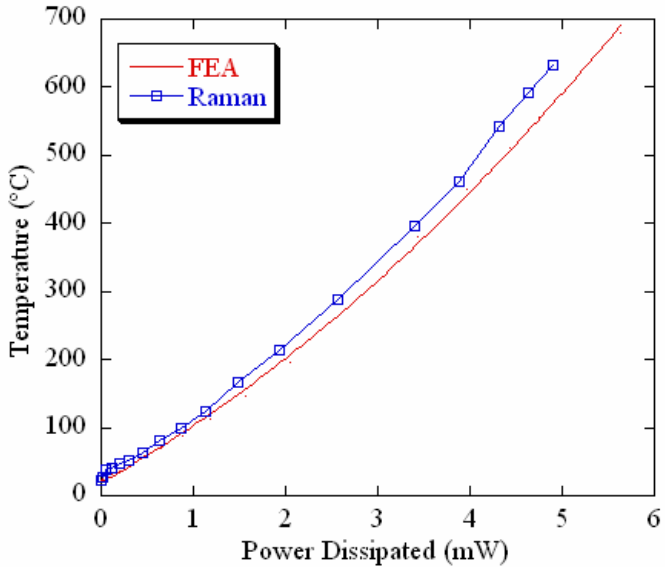

Figure 54. Experimental and FEA comparison of cantilever thermal response. Measurements were taken with increasing device power at the center of the heater section.

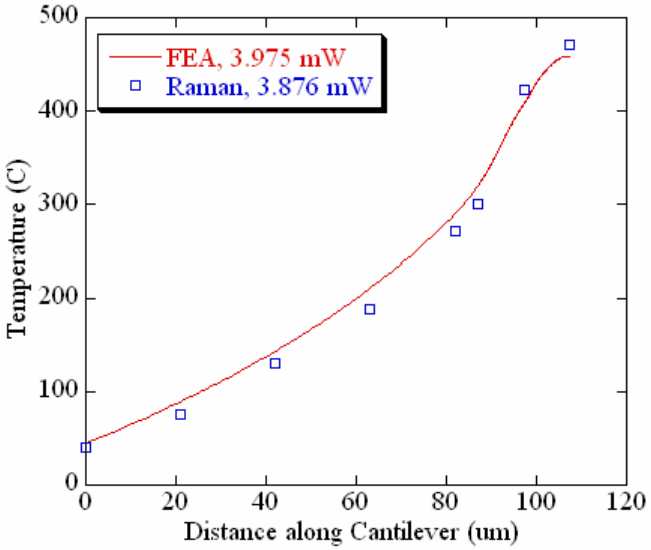

Figure 55. Experimental and FEA comparison of cantilever temperature distribution using half-symmetry.

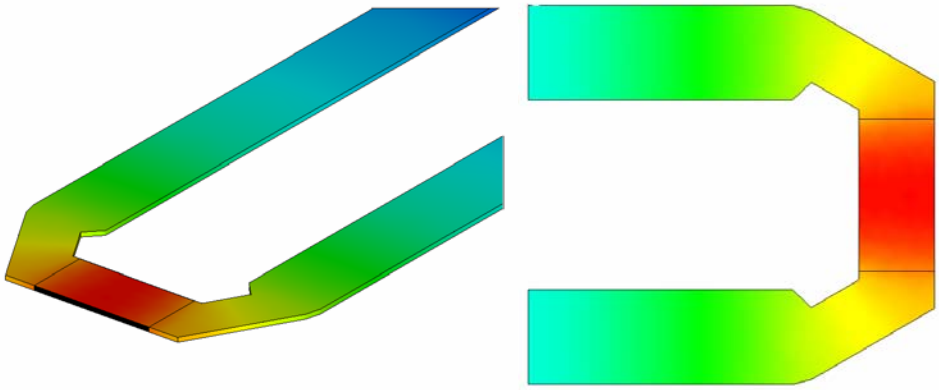

Figure 56. Typical temperature distribution of heated AFM cantilever from FEA. Left: 3-D full view. Right: Heater region top view.

Thermal response comparison of the calculated and Raman results of Sample 1A yield temperature agreement within 6% for the entire test regime. Again, the excellent agreement provides additional evidence of FEA model verification using Raman

thermometry. Figure 58 provides both a typical cross-sectional view of the heated micro-beam with heat conduction to the environment (left), and the temperature distribution along the beam length.

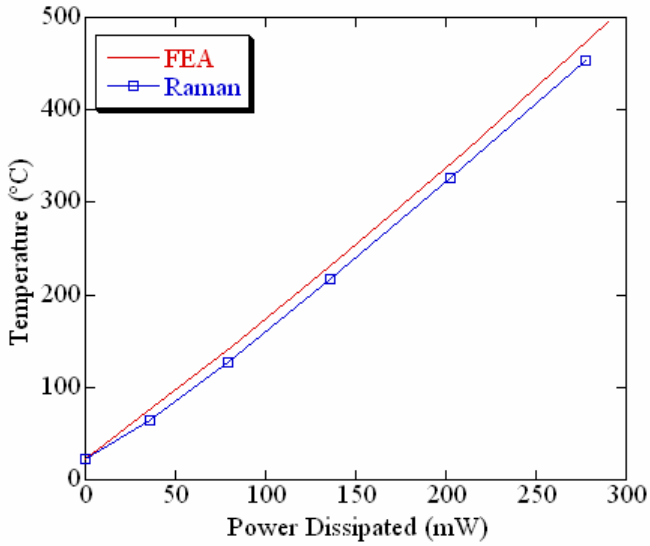

Figure 57. Experimental and FEA comparison of micro-beam on oxide (sample 1A) thermal response. Measurements were taken at the center of the beam.

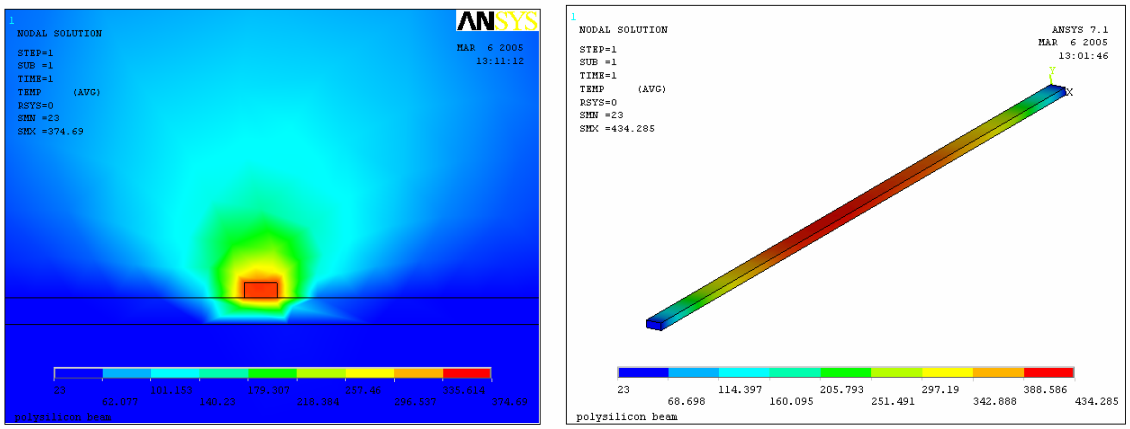

Figure 58. Typical temperature distribution of micro-beam from FEA. Left: profile view showing heat conduction into environment. Right: Temperature distribution along beam length.

Overall, the modeling shows good agreement with the experimental Stokes temperature measurements without the correction for stress being made. The FEA modeling provides additional evidence that the Stokes shift method may be used as a quick technique for mapping the temperature in some silicon MEMS devices without extensive calibrations. Additional material data and work is needed to model the behavior of stress in these devices with FEA. The effects of the change in these constraints for thermal MEMS devices are difficult to model due to uncertainty in high temperature mechanical properties. However, additional investigation of this effect is warranted.

CHAPTER VII

CONCLUSION AND FUTURE WORK

7.1 Conclusions

In this study, the main objective was to characterize Raman Spectroscopy as a micro-thermometry technique for Silicon-based MEMS Devices. Steady state temperature of doped silicon and polysilicon thermal devices was measured experimentally, with a spatial resolution range of 500-1000 nm, using three calibration techniques. By comparing these techniques, insight to experimental validation and the monitoring of hydrostatic stresses was gained. Finite element analysis was verified using Raman experimentation on three device types, permitting the acceptance of modeling for thermal MEMS design and reliability studies.

Temperature and stress were calibrated for a variety of single crystal and polycrystalline silicon materials. Linear coefficients were obtained when monitoring the Stokes peak shift for temperatures up to 1000ºC and uniaxial stresses between -300 and +300 MPa. Process parameters caused larger variations in the stress coefficients; however, the effect of temperature dominated that of stress on the Raman signature. Deviations amongst the materials were within the measurement uncertainty noise.

Parameters which affect the Raman thermometry technique were reported and elucidated. This includes aspects such as laser heating, spatial and spectral resolution, light collection efficiency, measurement uncertainty, and instrumental drift. This in-depth analysis helped to establish the accuracy of Raman thermometry for MEMS.

Uncertainty analysis revealed that for device temperatures of up to 500ºC, a single measurement using the Stokes shift method is accurate within ±5ºC, which utilizes a simple linear calibration and excellent repeatability. It was shown that thermally induced stresses can affect the Stokes position measurement, thus measurements of temperature, independent of stress, were attempted by calibrating other Raman signature features. The ratio of the Stokes to anti-Stokes signal intensities yielded a low range of sensitivity, large uncertainties (±22ºC), and long integration times for thermometry. By monitoring the Stokes linewidth, a combination of the advantages of both the Stokes frequency and intensity was realized. Anti-Stokes information is not necessary, decreasing integration times, and smaller uncertainties (±10ºC) are present in the steady state measurement. Studies compared all three calibration methods on thermal MEMS devices with a variety of boundary conditions. Experimental Stokes frequency yielded temperature agreement within 10% when compared to the intensity ratio methodology and a deviation of 7% from the Stokes linewidth data. The differences in the calibrations were attributed to thermal stress, and attempts were made to quantify device mechanical behavior.

Experimental data were used to validate finite element analysis models of the measured devices. Electrical and thermal responses were used as criteria for the comparison. Both temperatures as a function of power at a single device location and temperature distributions were compared, with maximum deviations of 9-10% seen. Only steady state responses were evaluated, although transient analysis is readily available by slightly modifying the FEA code.

7.2 Suggestions for Future Work

This research examines devices made of silicon, both doped and undoped. Raman is capable of monitoring other common MEMS materials such as Silicon Germanium, Silicon Nitride, diamond, and Silicon Carbide, depending on their crystallinity. Additional challenges occur in Silicon Nitride due to photoluminescence and weak scattering mechanisms. It is advisable to use longer wavelength laser excitation for such work. In the III-V semiconductor field, thermal metrology methods for materials such as Gallium Nitride, Zinc Oxide, and Gallium Arsenide are areas in need of additional research and are applicable to wide band gap semiconductors, especially light emitting devices. Temperatures in wide band gap semiconductors are expected to be much higher than those seen in Si-microelectronics and would fall well within the range of the capabilities of Raman thermometry. For light emitting applications, care must be taken to ensure that the laser excitation is far removed from the emission lines of the devices; UV-Raman may be most applicable for this situation.

Raman thermometry has shown some interesting indications of begin able to simultaneously measure both stress and temperature in microdevices; a first of its kind. Additional work is needed in understanding uncertainties and methods to accurately asses stress effects on Stokes frequency shift and linewidth. A study performing FEA of the mechanical response of the micro-beams and thermal AFM cantilevers would give additional insight into thermally induced stresses in such devices. This would require experimentation to obtain Young's Modulus and Poisson's ratio data for the doped polysilicon. It is possible to predict the hydrostatic stress in heated structures using Raman, however model verification would aid in the determination of stress distributions.

Accurate knowledge of the dopant concentration would contribute to more accurate resistivity data in FEA modeling. While SSUPREM3 provides a predication of this, it is desired to measure the concentration experimentally. SIMS (Secondary Ion Mass Spectroscopy) is a technique that can resolve dopant atom concentrations as a function of depth in a lattice. The technique analyzes atomic concentration as a function of depth by sputtering away atoms several monolayers at a time. A mass spectrometer is used measures the concentration of the removed atom species, providing excellent sensitivity.

Current design of a front-side illuminated CCD permits a quantum efficiency of roughly 20-40% with the 488 nm laser line [67]. The use of backside-illuminated detectors can provide improvements up to 75%. The photon collection time of a system is also limited by the mechanical shutter speed of the CCD. Both factors limit this technique to steady state temperature measurements. Surface enhanced Raman Spectroscopy (SERS) has the potential to provide an increased temporal signal response using non-evasive methods. It is known that the electron cloud surrounding metallic atoms, when brought in close proximity to a covalently bonded material, can enhance the scattered electric field from the sample. Following near-field techniques, an AFM with a metallized tip can be brought in close proximity of a thermal MEMS surface. With the aid of an intensified CCD camera, spectra with suitable signal-to-noise ratios can be measured at an increased rate. A temporal resolution on the order of several hundred microseconds is expected from this setup. This will provide suitable time scales for the transient analysis of most thermal MEMS devices. Initial efforts to implement this

technology with thermal MEMS devices are currently in progress, under the Georgia Tech-Sandia collaboration.

REFERENCES

1. Huang, Q. and N.K.S. Lee, *Analysis and Design of Polysilicon Thermal Flexure Acturator.* Journal of Micromechanics and Microengineering, 1999. **9**(1): p. 64-70.

2. Kolesar, E.S., P.B. Allen, J.T. Howard, J.M. Wilken, and N. Boydston, *Thermal-Actuated Cantilever Beam for Achieving Large in-plane Mechanical Deflections.* Thin Solid Films, 1999. **355-356**: p. 295-302.

3. Comtois, J.H., M.A. Michalicek, and C.C. Barron, *Electrothermal Actuators Fabricated in Four-Level Planarized Surface Mciromachined Polycrystalline Silicon.* Sensors and Actuators A, 1998. **70**: p. 23-31.

4. Mita, M., M. Arai, S. Tensaka, D. Kobayashi, and H. Fujita, *A Micromachined Impact Microactuator Driven by Electrostatic Force.* Journal of Microelectromechanical Systems, 2003. **12**(1): p. 37-41.

5. Que, L., J. Park, and Y.B. Gianchandani, *Bent-Beam Electrothermal Acturators-Part 1: Single Beam and Cascaded Devices.* Journal of Microelectromechanical Systems, 2001. **10**(2): p. 247-254.

6. Baker, M.S., R.A. Plass, T.J. Headley, and J.A. Walraven, *Final Report: Compliant Thermo-Mechanical MEMS Actuators LDRD #52553.* Sand Report SAND2004-6635, 2004: p. 1-38.

7. Park, J., L.L. Chu, A.D. Oliver, and Y.B. Gianchandani, *Bent-Beam Electrothermal Actuators-Part 2: Linear and Rotary Microengines.* Journal of Microelectromechanical Systems, 2001. **10**(2): p. 255-262.

8. Lott, C.D., T.W. McLain, J.N. Harb, and L.L. Howell, *Modeling the Thermal Behavior of a Surface-Micromachined Linear-Displacement Thermomechanical Microactuator.* Sensors and Actuators A, 2002. **101**: p. 239-250.

9. Graebner, J.E., S. Pau, and P.L. Gammel, *All-Optical Excitation and Detection of Microelectrical-Mechanical Systems.* Applied Physics Letters, 2002. **81**(19): p. 3531-3533.

10. Serrano, J.R., L.M. Phinney, and C.F. Brooks. *Laser-Induced Damage of Polycrystalline Silicon Optically Powered MEMS Actuators*. in *InterPACK*. 2005. San Fransico, CA.

11. Pan, C.S. and W. Hsu, *An Electro-Thermally and Laterally Driven Polysilicon Microactuator.* Journal of Micromechanics and Microengineering, 1997. **7**: p. 7-13.

12. Dumitrescu, M., C. Cobianu, D. Lungu, D. Dascalu, A. Pascu, S. Kolev, and A.v.d. Berg, *Thermal Simulation of Surface Micromachined Polysilicon Hot Plates of Low Power Consumption.* Sensors and Actuators, 1999. **76**: p. 51-56.

13. Weiller, B.H., P.D. Fugua, and J.V. Osborn, *Fabrication, Characterization, and Thermal Failure Analysis of a Micro Hot Plate Chemical Senor Substrate.* Journal of Electrochemical Society, 2004. **151**(3): p. H59-H65.

14. Mitzner, K.D., J. Sternhagen, and D.W. Galipeau, *Developement of a Micromachined Hazardous Gas sensor Array.* Sensors and Actuators B, 2003. **93**: p. 92-99.

15. D. Briand, A.K., B. van der Schoot, U. Weimar, N. Barsan, W. Gopel, N. F. de Rooij, *Design and Fabrication of High-Temperature Micro-Hotplates for Drop-Coated Gas Sensors.* Sensors and Actuators B, 200. **68**: p. 223-233.

16. King, W.P. and K.E. Goodson, *Thermal Writing and Nanoimaging with a Heated Atomic Force Microscope Cantilever.* Journal of Heat Transfer, 2002. **124**: p. 597.

17. King, W.P., T.W. Kenny, K.E. Goodson, G.L.W. Cross, M. Despont, U. Dürig, H. Rothuizen, G.K. Binnig, and P. Vettiger, *Design of Atomic Force Microscope Cantilevers for Combined Thermomechanical Writing and Reading in Array Operation.* Journal of Microelectromechanical Systems, 2002. **11**: p. 765-774.

18. Sheehan, P.E., L.J. Whitman, W.P. King, and B.A. Nelson, *Nanoscale Deposition of Solid Inks via Thermal Dip Pen Nanolithography.* Applied Physics Letters, 2004. **85**(9): p. 1589-1591.

19. Bullen, D., M. Zhang, and C. Lui. *Thermo-Mechanical Optimization of Thermally Actuated Cantilever Arrays*. in *SPIE Int Soc Opt Eng*. 2002. San Diego, CA.

20. Wright, T.L., *Fabrication and Testing of Heated Atomic Force Microscope Cantilevers*, MSME 2005, Georgia Institute of Technology: Atlanta, GA. p. 1-111.

21. Ajayan, P.M. and O. Zhou, *Applications of Carbon Nanotubes.* Carbon Nanotubes, 2000.

22. Englander, O., D. Christensen, and L. Lin, *Local Synthesis of Silicon Nanowires and Carbon Nanotubes on Microbridges.* Applied Physics Letters, 2003. **82**: p. 4797-4799.

23. Livermore, C., A.R. Forte, T. Lyszczarz, S.D. Umans, A.A. Ayon, and J.H. Lang, *A High-Power MEMS Electric Induction Motor.* Journal of Microelectromechanical Systems, 2004. **13**(3): p. 465-471.

24. Epstein, A.H., *Millimeter-Scale, Micro-Electro-Mechanical Systems Gas Turbine Engines.* Journal of Engineering for Gas Turbines and Power, 2004. **126**(2): p. 205-226.

25. Khanna, R., *MEMS Fabrication Perspectives from the MIT Microengine Project.* Surface and Coatings Technology, 2003. **163-164**: p. 273-280.

26. Zhang, Z.M., *Surface Temperature Measurements Using Optical Techniques.* Annual Review of Heat Transfer, 2000. **11**: p. 351-411.

27. Kolzer, J., E. Oesterschulze, and G. Deboy, *Thermal Imaging and Measurement Techniques for Electronic Materials and Devices.* Microelectronic Engineering, 1996. **31**: p. 251-270.

28. Gupta, S.C. *Materials for Infrared Photon Detectors: Status and Trends*. in *Proc. of SPIE*. 2000. New Dehli, India.

29. Rogalski, A., *Infrared Dectectors: Status and Trends.* Progress in Quantum Electronics, 2003. **27**(2-3): p. 59-210.

30. Trigg, A., *Applications of Infrared Microscopy to IC and MEMS Packaging.* IEEE Transactions on Electronics Packaging Manufacturing, 2003. **26**(3): p. 232-238.

31. Abedrabbo, S., J.C. Hensel, A.T. Fiory, B. Sopori, W. Chen, and N.M. Ravindra, *Perspective on Emissivity Measurements and Modeling in Silicon.* Materials Science in Semiconductor Processing, 1998. **1**: p. 187-193.

32. Tallant, D.R., T.J. Headley, J.W. Medernach, and F. Geyling. *Characterization of Polysilicon Films by Raman Spectroscopy and Transmission Electron Microscopy: A Comparative Study*. in *Materials Research Society*. 1993.

33. Hefner, A., D. Berning, D. Blackburn, C. Chapuy, and S. Bouche, *A High-Speed Thermal Imaging System for Semiconductor Analysis.* Annual IEEE Semiconductor Thermal Measurement and Management Symposium, 2001: p. 43-49.

34. Fletcher, D.A., K.B. Crozier, C.F. Quate, G.S. Kino, K.E. Goodson, D. Simanovskii, and D.V. Palanker, *Near-Field Infrared Imaging with a Microfabricated Solid Immersion Lens.* Applied Physics Letters, 2000. **77**: p. 2109-2111.

35. Boudreau, B.D., J. Raja, R.J. Hocken, S.R. Patterson, and J. Patten, *Thermal Imaging with Near-Field Microscopy.* Review of Scientific Instruments, 1997. **68**: p. 3096-3098.

36. Zhao, Y., M. M, R. Horowitz, A. Majumdar, J. Varesi, P. Norton, and J. Kitching, *Optomechanical Uncooled Infrared Imaging System: Design, Microfabrication, and Performance.* Journal of Microelectromechanical Systems, 2002. **11**: p. 136-146.

37. Luerssen, D., J.A. Hudgings, P.M. Mayer, and R.J. Ram. *Nanoscale Thermoreflectance with 10mK Temperature Resolution Using Stochastic Resonance*. in *Semi-Therm 21*. 2005. San Jose, CA.

38. Cahill, D.G., K. Goodson, and A. Majumdar, *Thermometry and Thermal Transport in Micro/Nanoscale Solid-State Devices and Structures.* Journal of Heat Transfer, 2002. **124**: p. 223-241.

39. Goodson, K.E. and Y.S. Ju, *Short-Time-Scale Thermal Mapping of Microdevices Using a Scanning Thermoreflectance Technique.* Journal of Heat Transfer, 1998. **20**: p. 306-313.

40. Ju, Y.S., O.W. Kading, Y.K. Leung, S.S. Wong, and K.E. Goodson, *Short-Timescale Thermal Mapping of Semiconductor Devices.* Electron Device Letters, 1997. **18**(5): p. 169-171.

41. Fournier, D., B.C. Forget, C. Boue, and J.P. Roger, *Micron Scale Photothermal Imaging.* International Journal of Thermal Sciences, 2000. **39**: p. 514-518.

42. Grauby, S., S. Dilhaire, S. Jorez, and W. Claeys, *Temperature Variation Mapping of a Microelectromechanical System by Thermoreflectance Imaging.* Electron Device Letters, 2005. **26**(2): p. 78-80.

43. Dilhaire, S., S. Grauby, and W. Claeys, *Calibration Procedure for Temperature Measurements by Thermoreflectance under High Magnification Conditions.* Applied Physics Letters, 2004. **84**(5): p. 822-824.

44. Hohlfeld, J., J.G. Muller, S.S. Wellershoff, and E. Matthias, *Time-Resolved Thermoreflectivity of Thin Gold Films and its Dependance on Film Thickness.* Applied Physics B, 1997. **64**: p. 387-390.

45. Shi, L., O. Kwon, G. Wu, and A. Majumdar. *Quantitative Thermal Probing of Devices at Sub-100 nm Resolution*. in *IEEE International Reliability Physics*. 2000. San Jose, CA.

46. Cannaerts, M., E. Seynaeve, G. Rens, A. Volodin, and C.V. Haesendonck, *Implementation and Optimization of a Scanning Joule Expansion Microscope for*

the Study of Small Conducting Gold Wires. Applied Surface Science, 2000. **157**: p. 308-313.

47. Varesi, J. and A. Majumdar, *Scanning Joule Expansion Microscopy at Nanometer Scales.* Applied Physics Letters, 1998. **72**: p. 37-39.

48. Majumdar, A., *Scanning Thermal Microscopy.* Annual Review of Materials Science, 1999: p. 505-585.

49. Goss, L.P., A.A. Smith, and M.E. Post, *Surface Thermometry by Laser Induced Fluorescence.* Review of Scientific Instruments, 1998. **60**: p. 3702-3706.

50. Keuren, E.V., M. Cheng, O. Albertini, C. Luo, J. Currie, and M. Paranjape, *Temperature profiles of microheaters using fluorescence microthermal imaging.* Sensors and Materials, 2005. **17**(1): p. 1-6.

51. Femicola, V.C., L. Rosso, R. Galleano, T. Sun, Z.Y. Zhang, and K.T.V. Gratton, *"Investigations on Exponential Lifetime Measurements for Fluorescence Thermometry.* Review of Scientific Instruments, 2000. **71**: p. 2938-2943.

52. Oh, C., G. Coles, and W.N. Sharpe. *High Temperature Behavior of Polysilicon*. in *Materials Research Society Symposium*. 2002. Boston, MA.

53. Cui, J.B., K. Amtmann, J. Ristein, and L. Ley, *Noncontact Temperature Measurements of Diamond by Raman Scattering Spectroscopy.* Journal of Applied Physics, 1998. **83**: p. 7929-7933.

54. Viera, G., S. Huet, and L. Boufendi, *Crystal Size and Temperature Measurements in Nanostructured Silicon Using Raman Spectroscopy.* Journal of Applied Physics, 2001. **90**: p. 4175-4183.

55. Ostermeir, R., K. Brunner, G. Abstreiter, and W. Weber, *Temperature Distribution in Si-MOSFET's Studied by Micro Raman Spectroscopy.* Transactions on Electron Devices, 1992. **39**: p. 858-863.

56. Perichon, S., V. Lysenko, B. Remaki, D. Barbier, and B. Champagnon, *Measurement of Porous Silicon Thermal Conductivity by Micro-Raman Scattering.* Journal of Applied Physics, 1999. **86**: p. 4700-4702.

57. Brugger, H. and P.W. Epperlein, *Mapping of Local Temperatures on Mirrors of GaAs/AlGaAs Laser Diode.* Applied Physics Letters, 1990. **56**: p. 1049-1051.

58. Epperlein, P.W., G.L. Bona, and P. Roentgen, *Local Mirror Temperatures of Red-Emitting (Al)GalnP Quantum Well Laser Diodes by Raman Scattering and Reflectance Modulation Measurements.* Applied Physics Letters, 1992. **60**(6): p. 680-682.

59. Kuball, M., S. Rajasingam, A. Sarua, M. Uren, T. Martin, B.T. Hughes, K.P. Hilton, and R. Balmer, *Measurement of Temperature Distribution in Multifinger AlGaN/GaN Heterostructure Field-Effect Transistors using Micro-Raman Spectroscopy.* Applied Physics Letters, 2003. **82**(1): p. 124-126.

60. Chitnis, A., J. Sun, V. Mandavilli, R. Pachipulusu, M.G. S. Wu, V. Adivarahan, J. Zhang, M.A. Khan, A. Sarua, and M. Kuball, *Self-heating Effects at high Pump Currents in Deep Ultraviolet Light-Emitting Diodes at 324 nm.* Applied Physics Letters, 2002. **81**: p. 3491-3493.

61. Bowden, M. and D. Gardiner, *High Resolution Raman Shift and Bandwidth Images of Stressed Silicon.* Internet Journal of Vibrational Spectroscopy, 1998. **2**.

62. Starman, L.A., J.A. Lott, M.S. Amer, W.D. Cowan, and J.D. Busbee, *Stress Characterization of MEMS Microbridges by Micro-Raman Spectroscopy.* Sensors and Actuators, 2003. **104**: p. 107-116.

63. Lourenco, M.A., D.J. Gardiner, and M. Bowden, *Stress Analysis of B Doped Silicon Bridges and Cantilever Structures by Raman Spectrscopy.* Journal of Materials Science Letters, 2000. **19**: p. 767-769.

64. Bowden, M., D. Gardiner, D. Wood, J. Burdess, A. Harris, and J. Hedley, *Raman and Finite-Element Analysis of a Mechincally Strained Silicon Microstructure.* Journal of Micromechanics and Microengineering, 2001. **11**: p. 7-12.

65. Raman, C.V. and K.S. Krishnan, *A New Type of Radiation.* Nature, 1928. **121**(501).

66. Lewis, I.R. and H.G.M. Edwards, *Handbook of Raman Spectroscopy.* 2001: p. 11-40.

67. McCreery, R.L., *Raman Spectroscopy of Chemical Analysis*. 2000, New York, NY: John Wiley & Sons.

68. Eckbreth, A.C., *Laser Diagnostics for Combustion Temperature and Species*. 1988, Cambridge: Abacus Press.

69. Bowden, M., D.J. Gardiner, A.A. Parr, R.T. Carline, R.J. Bozeat, R.J.T. Bunyan, and M. Ward. *Temperature Mapping of Polysilicon Microheaters using Raman Spectroscopy*. in *Inst. Conf. Ser. No. 157*. 1997.

70. Niitsu, Y., T. Ikeda, and T. Tadokoro, *Accuracy Evaluation of Stress Measurement in Silicon Crystal by Microscopic Raman Spectroscopy.* Advances in Electronic Packaging, 1993. **4-1**: p. 255-259.

71. L. A. Starman Jr., J.A.L., M. S. Amer, W. D. Cowan, J. D. Busbee, *Stress Characterization of MEMS Microbridges by Micro-Raman Spectroscopy.* Sensors and Actuators, 2003. **104**: p. 107-116.

72. Zouboulis, E.S. and M. Grimsditch, *Raman Scattering in Diamond up to 1900 K.* Physical. Review B, 1991. **43**(15): p. 490-493.

73. Nickel, N.H., P. Lengsfeld, and I. Sieber, *Raman Spectroscopy of Heavily Doped Polycrystalline Silicon Thin Films.* Physical Review B, 2000. **61**: p. 558-561.

74. Chen, J. and I.D. Wolf, *Study of Damage and Stress Induced By Backgrinding in Si Wafers.* Semiconductor Science and Technology, 2003. **18**: p. 261-268.

75. M. Kuball, S.R., A. Sarua, M. Uren, T. Martin, B. T. Hughes, K. Hilton, R. Balmer, *Measurement of Temperature Distribution in Multifinger AlGaN/GaN Heterostructure Field-Effect Transistors Using Micro-Raman Spectroscopy.* Applied Physics Letters, 2003. **82**: p. 124-126.

76. Balkanski, M., R.F. Wallis, and E. Haro, *Anharmonic Effects in Light Scattering Due to Optical Phonons in Silicon.* Physical Review B, 1983. **28**(4): p. 28-34.

77. Herchen, H. and M.A. Cappelli, *First-Order Raman Spectrum of Diamond at High Temperatures.* Physical Review B, 1991. **43**(14): p. 740-744.

78. McCarthy, B., Y. Zhao, R. Grover, and D. Sarid, *Enhanced Raman Scattering for Temperature Measurement of a Laser-Heated Atomic Force Microscope Tip.* Applied Physics Letters, 2005. **86**.

79. Abel, M.R., T.L. Wright, E.O. Sunden, S. Graham, W.P. King, and M.J. Lance. *Thermal Metrology of Silicon Microstructures using Raman Spectroscopy*. in *Semi-therm 21*. 2005. San Jose, CA.

80. Dietrich, B., V. Bukalo, A. Fischer, K.F. Dombrowski, E. Bugiel, B. Kuck, and H.H. Richter, *Raman-Spectroscopic Determination of Inhomogeneous Stress in Submicron Silicon Devices.* Applied Physics Letters, 2003. **82**(8): p. 1176-1178.

81. Paillard, V., P. Puech, and P.R. Cabarrocas, *Measurement of Stress Gradients in Hydrogenated Microcrystalline Silicon Thin Films using Raman Spectroscopy.* Journal of Non-Crystalline Solids, 2002. **299-302**: p. 280-283.

82. Jellison, G.E., M. Keefer, and L. Thornquist. *Spectroscopic Ellipsometry and Interference Reflectometry Meausurements of CVD Silicon Grown on Oxidized Silicon*. in *Materials Research Society*. 1993.

83. Parr, A.A., C. Bodart, D. Demonchy, and D.J. Gardiner, *Depth Profiling Variously Deposited LPCVD Polysilicon Films using Raman Microscopy.*

Semiconductor Science and Technology, 2001. **16**: p. 608-613.

84. Kearney, S., *Spectral Peak Fitting Code*. 2005: Albuquerque, NM.

85. Kamins, T., *Polycrystalline Silicon for Integrated Circuits and Displays*. 1998: Springer.

86. McConnell, A.D., S. Uma, and K.E. Goodson, *Thermal Conductivity of Doped Polysilicon Layers.* Journal of Micromechanical Systems, 2001. **10**(3): p. 360-369.

87. Incropera, F.P. and D.P. DeWitt, *Introduction to Heat Transfer, 4th Ed.* 2002, New York, NY: Wiley & Sons. 892.

88. Olson, B., S. Graham, and K. Chen, *A Practical Extension of the 3-w Method to Multilayer Structures.* Review of Scientific Instruments, 2005. **76**(5): p. 53901-1-7.

89. Reggiani, S., M. Valdinoci, L. Colalongo, M. Rudan, and G. Baccarani, *An Analytical, Temperature-Dependant Model for Majority-and Minority-Carrier Mobility in Silicon Devices.* VLSI Design, 2000. **10**(4): p. 467-483.

90. Guo, Z., Z. Li, and X. Luo. *Size Effect on Free Convection in a Square Cavity*. in *International Symposium on Micro/Nanoscale Energy Conversion and Transport*. 2002. Antalya, Turkey.